

**Arab American University
Faculty of Graduate Studies
Department of Health Sciences
Master Program in Physics**



**Structural Analysis of Doped BZN Pyrochlore Ceramics as a
Function of Temperature Using Synchrotron Radiation**

Rama Watheq Najeeb Hithnawi

202020350

Supervision Committee:

Assoc. Prof. Dr. Adli Saleh

Assoc. Prof. Dr. Muayyad Abu Saa'

Prof. Dr. Zaki Saleh

Assoc. Prof. Dr. Mohammad Elsaid

**This Thesis Was Submitted in Partial Fulfilment of the
Requirements for the Master Degree in Physics.**

Palestine, 9/2024

© Arab American University. All rights reserved.

Arab American University
Faculty of Graduate Studies
Department of Health Sciences
Master Program in Physics



Thesis Approval

Structural Analysis of Doped BZN Pyrochlore Ceramics as a Function of Temperature Using Synchrotron Radiation

Rama Watheq Najeeb Hithnawi

202020350

This thesis was defended successfully on 19/9/2024 and approved by:

Thesis Committee Members:

Name	Title	Signature
1. Assoc. Prof. Dr. Adli Saleh	Main Supervisor	
2. Assoc. Prof. Dr. Muayyad Abu Saa'	Members of Supervision Committee	
3. Prof. Dr. Zaki Saleh	Members of Supervision Committee	
4. Assoc. Prof. Dr. Mohammad Elsaid	Members of Supervision Committee	

Palestine, 9/2024

Declaration

I declare that, except where explicit reference is made to the contribution of others, this thesis is substantially my own work and has not been submitted for any other degree at the Arab American University or any other institution.

Student Name: Rama Watheq Najeeb Hithnawi

Student ID: 202020350

Signature: Rama Hithnawi

Date of Submitting the Final Version of the Thesis: 23/1/2025

Dedication

To Allah

Rama Watheq Najeeb Hithnawi

Acknowledgments

First of all, all thanks to Allah for giving me the full strength to finish this thesis.

A special debt of gratitude is owed to my supervisors: Assoc. Prof. Dr. Adli Saleh and Assoc. Prof. Dr. Muayyad Abu Saa' for their precious support and great help during my work as their student. Great thanks are also given to Prof. Atef Qasrawi for his assistance in analyzing Data. Great gratitude to Dr. Mahmoud Alstaty who reviewed my thesis to make sure it is written in a good scientific language. I would extend my deep thanks to all of my instructors at physics department: Prof. Dr. Zaki Saleh, Mr. Anan Hussein, Assoc. Prof. Dr. Ahmad Omar, Prof. Dr. Mohammad Abu Samreh and Dr. Sulaiman Rabbaa'. I wish to express my sincere thanks to Dr. Mahmoud Abdellatief, who is the MS/XPD Beamline Principal Scientist at SESAME.

I express my gratitude to my husband Mohammad who continuously supported me and always believed in me. Thank you is a small word for all that you have done for me. This work is dedicated to my children: Sama & Mahmoud, you have made me stronger and more fulfilled more than I could have ever imagined.

I offer my gratitude to my family, for their unconditional love and support during all stages of my study life. To my parents, Eng. Wafa' and Eng. Watheq. I would not have become what I am today without their care and support. They are the best parents in the world and I owe all of my successes to them. I am also grateful to my sisters and brothers, Amr, Basmalah, Taibah and Mohammad for always being there for me. Also, special thanks go to my best friend Tahani for always telling me that I can do it.

Structural Analysis of Doped BZN Pyrochlore Ceramics as a Function of Temperature Using Synchrotron Radiation

Rama Watheq Najeeb Hithnawi

Assoc. Prof. Dr. Adli Saleh

Assoc. Prof. Dr. Muayyad Abu Saa'

Prof. Dr. Zaki Saleh

Assoc. Prof. Dr. Mohammad Elsaid.

Abstract

In this thesis, the structural properties of $\text{Bi}_{1.5}\text{Zn}_{0.92}\text{Nb}_{1.5}\text{O}_{6.92}$ pyrochlore ceramics doped with Cr, Ni and In were investigated using synchrotron radiation at SESAME. Changes in the interplaner spacing, lattice constant, micro-strain, crystallite size and dislocation density were studied. In the first part of this study, Cr, Ni and In doped BZN pyrochlore ceramics were studied at room temperature (RT). The lattice constant value obtained decreases with increasing the Ni content and increases with increasing the In content in the sample. The change in the lattice constant with changing the dopant content was interpreted as a result of the different ionic radius of the dopant atom. No new phases have been observed in these samples since they remained under the solubility limit. In the second part of this study, (0.10) Cr and (0.10) Ni doped BZN pyrochlore ceramics were studied in a temperature range of (RT-600) $^{\circ}\text{C}$, in a step of 25 $^{\circ}\text{C}$. It was observed that as temperature increases, the maximum peak shifts to lower angles increasing the lattice constant value gradually. In addition, increasing temperature have led to a greater shift in the peak at higher Bragg's angles, which is attributed to the increase in the lattice constant with increasing temperature from 10.5485 $^{\circ}\text{A}$ to 10.5770 $^{\circ}\text{A}$ for the (0.10) Cr doped BZN, and from 10.5627 $^{\circ}\text{A}$ to 10.5985 $^{\circ}\text{A}$ for the (0.10) Ni doped BZN. For the (0.10) Ni doped BZN pyrochlore, seven new XRPD peaks appeared at 25.57478 $^{\circ}$, 35.17912 $^{\circ}$, 43.40210 $^{\circ}$, 52.60903 $^{\circ}$, 66.61307 $^{\circ}$, 76.94071 $^{\circ}$ and 95.34664 $^{\circ}$. The first three peaks were found to originate from Nb_2O_5 , ZnO, and NiO phases respectively, while the rest of the seven new peaks are due to dislocations and stacking faults in the crystal structure of the sample. Finally, Thermal Expansion Coefficient (TEC) was calculated to be $4.9124 \times 10^{-6} \left(\frac{1}{^{\circ}\text{C}}\right)$ for the (0.10) Cr doped BZN pyrochlore ceramic and $6.1623 \times 10^{-6} \left(\frac{1}{^{\circ}\text{C}}\right)$ for the (0.10) Ni doped BZN pyrochlore ceramic.

Keywords: pyrochlore ceramics, XRPD, synchrotron radiation, Thermal Expansion Coefficient.

Table of Contents

#	Title	Page
	Declaration	I
	Dedication	II
	Acknowledgments	III
	Abstract	IV
	List of Tables	VII
	List of Figures	VIII
	List of Definitions of Abbreviations	XII
Chapter One	Introduction	1
Chapter Two	Theoretical background	3
2.1	Ceramics	3
2.1.1	Properties of ceramics	5
2.1.2	Applications of ceramics	6
2.1.3	Pyrochlore ceramics	9
2.2	X-ray	10
2.2.1	X-ray generation	10
2.2.2	X-ray diffraction	12
2.2.2.1	Bragg's law	13
2.2.2.2	X-ray powder diffraction	15
2.2.2.3	XRD parameters	16

2.3	Synchrotron light source	21
2.3.1	A general glimpse about Synchrotron facilities	22
2.3.2	Synchrotron light properties	24
2.3.3	Synchrotron machine at SESAME	25
Chapter Three	Experimental Details	34
3.1	Doped Bi _{1.5} Zn _{0.92} Nb _{1.5} O _{6.92} Ceramics Preparation	34
3.2	Material Science-X Ray Powder Diffraction (MS-XPD) beamline	39
Chapter Four	Results and discussion	46
4.1	Structural properties for samples studied at RT	46
4.2	Structural properties for samples studied at high HT (RT-600) C°	49
4.2.1	(0.10) Cr doped BZN pyrochlore	50
4.2.2	(0.10) Ni doped BZN	54
4.3	Thermal Expansion Coefficient (TEC)	61
Chapter Five	Conclusions	62
References		64
ملخص		68

List of Tables

Table #	Title of Table	Page
2.1	Properties of some polycrystalline ceramics.	6
2.2	Classification of ceramics based on the main function.	8
3.1	Showing the temperatures at which our samples were studied.	41
3.2	The cooling rate for the samples studied at high temperature.	45
4.1	Intensity of the maximum peak, 2θ of the maximum peak and the interplaner spacing for doped BZN pyrochlore ceramics as a function of doping level at room temperature.	47
4.2	Mechanical parameters for Cr, In and Ni doped BZN pyrochlores samples at room temperature.	48
4.3	Shows the origin of the seven new peaks appeared in the XRPD pattern at 600 C° for (0.10) Ni doped BZN pyrochlore ceramic sample.	57

Table of Figures

Figure #	Title of Figure	Page
2.1	General classification of ceramics.	4
2.2	Oxide and non-oxide ceramics categories.	5
2.3	The general structure of $A_2B_2O_7$ pyrochlore.	9
2.4	Simplified x-ray diagram.	11
2.5	Bremsstrahlung vs characteristic x-ray radiation.	12
2.6	Simple schematic diagram of x-ray diffraction.	13
2.7	Schematic diagram of Bragg's law.	14
2.8	Simulated and indexed powder X-ray diffraction pattern for bulk (1 μm) wurtzite CdS. The inset shows the crystal structure of wurtzite CdS with the (100), (002), and (101) planes highlighted.	15
2.9	Broad peak (in blue) and narrow peak (in red).	17
2.10	Steps of calculating the FWHM from an XRD pattern: A. Some peak at the max. intensity with specific 2θ , B. Illustration of $\frac{1}{2}$ the max. peak intensity and C. Illustration of min. 2θ value and the max 2θ value at $\frac{1}{2}$ the max. intensity.	17
2.11	Grain boundaries (black) and grains (yellow) in a polycrystal.	18
2.12	FCC (right) vs HCP (left) structure.	20
2.13	A scheme of synchrotron facility.	22
2.14	ANSTO's facility.	23
2.15	SESAME facility.	23
2.16	Synchrotron rang on the EM spectrum.	24

2.17	LINAC & e-gun.	25
2.18	The booster ring.	26
2.19	The storage ring.	27
2.20	Each type: a. dipole, b. quadrupole and c. sextupole shows poles & streamlines of magnetic field in transverse cross section. South (-ve electrostatic potential) & north (+ve electrostatic potential) poles are shown in blue and red.	28
2.21	The bending magnets of the storage ring.	28
2.22	A. dipole, the first type of bending magnets in the storage ring. B. the second type, Quadrupole, C. the third type, Sextupole. In the storage at SESAME, there are 16 dipoles, 64 Quadrupoles and 64 Sextupoles.	29
2.23	Insertion devices (IDs).	30
2.24	Part of the storage ring at SESAME including BMs & IDs.	31
2.25	RF system at SESAME in: A. the booster ring and B. the storage ring	32
2.26	The Materials Science-X-ray Powder Diffraction (MS/XPD) beamline at SESAME.	33
3.1	Ball milling method for mixing. [38]	35
3.2	A. Compacted product, B. Partly sintered product. [39]	36
3.3	Cr doped BZN samples attached with Sintering and calcination temperatures.	37

3.4	Mortar and pestle to crush ceramics pellets into fine powder.	37
3.5	In doped BZN samples attached with the sintering temperature.	38
3.6	Ni doped BZN samples attached with calcination and sintering temperatures.	39
3.7	The optical layout of the MS/XPD beamline at SESAME.	40
3.8	The diffractometer used in MS/XPD beamline at SESAME.	41
3.9	Quartzkapillaren (the red one) and borokapillaren (the green one).	42
3.10	Electrocautery device (on right) & (vibrator) (on left).	43
3.11	The capillary spinner used to fix the sample.	43
3.12	The experimental room at SESAME.	44
4.1	XRPD patterns of $\text{Bi}_{1.5}\text{Zn}_{0.92}\text{Nb}_{1.5}\text{O}_{6.92}$ pyrochlore doped with (Cr, Ni and In) at room temperature.	46
4.2	Three dimensional temperature dependent XRPD patterns of (0.10) Cr doped BZN pyrochlore from 50 C° to 600 C° in step of 100 C° and in 2θ range of (10°-90°).	50
4.3	Temperature dependent XRPD patterns of (0.10) Cr doped BZN pyrochlore from 50 C° to 600 C° in step of 25 C° and in 2θ range of (15°-160°).	51
4.4	Zooming in on the maximum peaks of (0.10) Cr doped BZN pyrochlore sample for temperature range of (50-600) C°.	52

4.5	$2\theta_{max}$ vs T in a temperature range of (50-525) °C for (0.10) Cr doped BZN pyrochlore ceramic.	52
4.6	The variation of the: A. intensity of the maximum peak, B. crystallite size, C. micro-strain (μ), D. dislocation density δ , E. lattice constant and F. interplaner spacing with increasing temperature in a range of (50-600) °C of (0.10) Cr doped BZN pyrochlore ceramic.	54
4.7	Three dimensional temperature dependent XRPD patterns from 30 C° to 600 C° in a step of 100 C° and in 2θ range of (10°-90°).	55
4.8	Temperature dependent XRPD patterns from 30 C° to 600 C° in a step of 25 C° and in 2θ range of (12°-125°).	56
4.9	A comparison between the XRPD patterns of (0.10) Ni doped BZN at 30 C° and at 600 C° in 2θ range of (12°-125°).	56
4.10	Zooming in on the maximum peaks of 0.1 Ni doped BZN pyrochlore sample for temperature range of (30-600) C°.	58
4.11	$2\theta_{max}$ vs T in a temperature range of (30-575) °C for (0.10) Ni doped BZN pyrochlore ceramic.	58
4.12	The variation of the: A. intensity of the maximum peak, B. crystallite size, C. micro-strain (μ), D. dislocation density δ , E. lattice constant and F. interplaner spacing with increasing temperature in a range of (30-600) °C of (0.10) Ni doped BZN pyrochlore ceramic.	60

List of Definitions of Abbreviations

Abbreviations	Title
BZN	$\text{Bi}_{1.5}\text{Zn}_{0.92}\text{Nb}_{1.5}\text{O}_{6.92}$
VR	Visible Region
TBCs	Thermal Barrier Coatings
LTCC	Low Temperature Co-Fired Ceramic
MSE	Material Science and Engineering
HK	Knoop Hardness
Face-Centered Cubic	FCC
XRPD	X-ray Powder Diffraction
FWHM	Full Width at Half Maximum
HCP	Hexagonal Close Packed
TEC	Thermal Expansion Coefficient
EM	Electromagnetic
λ	Wavelength
d	Interplaner spacing
θ_i	Angle of incidence
θ_r	Angle of reflection
β	Peaks broadening
α	Thermal Expansion Coefficient
δ	Dislocation density
ε	Strain
n	Integer number

D	Crystallite size
θ	Diffraction angle
a	Lattice constant

Chapter One: Introduction

Today's accelerating technologies call for an enhancement in the optical, electrical, thermal, dielectric and structural properties of ceramics. Researchers tend to take advantage of pyrochlore ceramics as they have appropriate structures for doping with many elements without changing their own structure. A previous study has presented an overview of ceramic scintillators [1], the attention in this study is concentrated on Cerium doped gamma-ray scintillators that are important in medical imaging applications. Another study proposed the suitability of pyrochlores for Visible Region (VR) light optical applications as in photovoltaic devices [2]. Electrical properties of pyrochlores are particularly important because of their presence in varistor ceramics at the interfaces [3]. Also, pyrochlores can enhance the thermos-physical properties making them good for Thermal Barrier Coatings (TBCs) [4, 5]. In addition, the dielectric properties of pyrochlores make them promising materials to use in high frequency filter applications [6]. Studying the structural properties of pyrochlores at high temperatures is important as well, since it paves the way to new possible applications [7].

$\text{Bi}_{1.5}\text{Zn}_{0.92}\text{Nb}_{1.5}\text{O}_{6.92}$ (BZN) ceramic is one of the pyrochlores that has a wide range of applications. It can be used as radio/microwave band pass/reject filters [8]. Also, BZN thick films deposited on platinum foils can be exploited in flexible electronic devices [9]. Furthermore, another study discussed the possibility of developing BZN pyrochlore for microwave applications [10].

Many dopants have been used to enhance the considerable properties of BZN pyrochlores. As an example, conventional oxide mixed route has been used to prepare $\text{Bi}_2(\text{Zn}_{1-x}\text{Ni}_x)_{2/3}\text{Nb}_{4/3}\text{O}_7$ ceramics which exhibited improved dielectric properties, making them a suitable candidate of thermostable Low Temperature Co-Fired Ceramic (LTCC) materials [11]. In another study, solid state reaction technique was used to fabricate Tungsten doped BZN ceramic. Tungsten achieved an outstanding engineering in the dielectric, optical, electrical and structural properties of the pyrochlore ceramics. It was reported that the enhancement in the densification of the pyrochlore leading to larger crystallites growth and higher light absorbability is due to increasing the W content in the BZN pyrochlore [12]. Another work [13] involved the fabrication of Cr and Co doped BZN

ceramics which were prepared by solid state mixing of oxides. A decrease in the temperature coefficient with Cr doping versus an increase in it with Co doping was observed. All of the previously mentioned studies discussed how the structural properties are changed after doping the pyrochlores with many dopants, but no one involved studying the stability of the samples while changing a new factor, which is temperature. Additionally, a higher accuracy can be obtained when studying all of these mentioned properties taking the advantage of the high accuracy synchrotron light source.

Consequently, a motivation to this study is to investigate the structure of (0.10) Cr doped BZN and (0.10) Ni doped BZN pyrochlore ceramics at temperatures higher than the room temperature. In this work, In, Cr and Ni doped BZN pyrochlores were produced using solid-state reaction technique by mixing the proper amounts of oxides. Our goal is to investigate their structure via synchrotron light source that is expected to give more accurate results compared to the conventional XRD device opening our eyes to new phases and properties. Also, the structure of two of the samples (0.10 Cr & 0.10 Ni doped BZN) is studied as a function of temperature up to 600 C° with 25 C° step to investigate the thermal stability and to measure the Thermal Expansion Coefficient. It is expected that crystalline phases of Cr, Ni and In doped BZN samples will be produced. The heat treatment of (0.10) Cr and (0.10) Ni doped BZN samples is expected to enhance crystallinity, and that the synchrotron light source results will give more accurate x-ray diffraction patterns than the conventional XRD.

In this Chapter, we summarized the literature review about the research topic and identified the research gap. In Chapter 2, a theoretical background is presented. Experimental set-ups that were used in this work and the experimental steps we followed are all presented in Chapter 3. Our results are discussed and analyzed in Chapter 4. Future plans and perspectives are presented in Chapter 5.

Chapter Two: Theoretical background

2.1 Ceramics

In Material Science and Engineering (MSE), one way to classify materials is to divide them into five groups: metals and alloys, ceramics and glasses, polymers, semiconductors and composites. Each group has different structures and properties. In our research, we are interested in ceramics which are defined as inorganic solids of metallic and nonmetallic elements. They are generally classified into:

- Traditional ceramics: they are ceramics made from natural materials, like clay minerals or quartz sand. They are at most used to create brick and clay tile, industrial abrasives and refractory linings. What affects their quality control is having more imperfections.
- Advanced ceramics: they are all the products made from high purity, inorganic compounds through manufacturing specialized processes. Due to their insulation, conduction, magnetism and permeability, advanced ceramics can be used for many purposes. The microstructure of advanced ceramics is uniform and without imperfections or impurities since their structure can be modified by changing the chemical compound used to construct it.

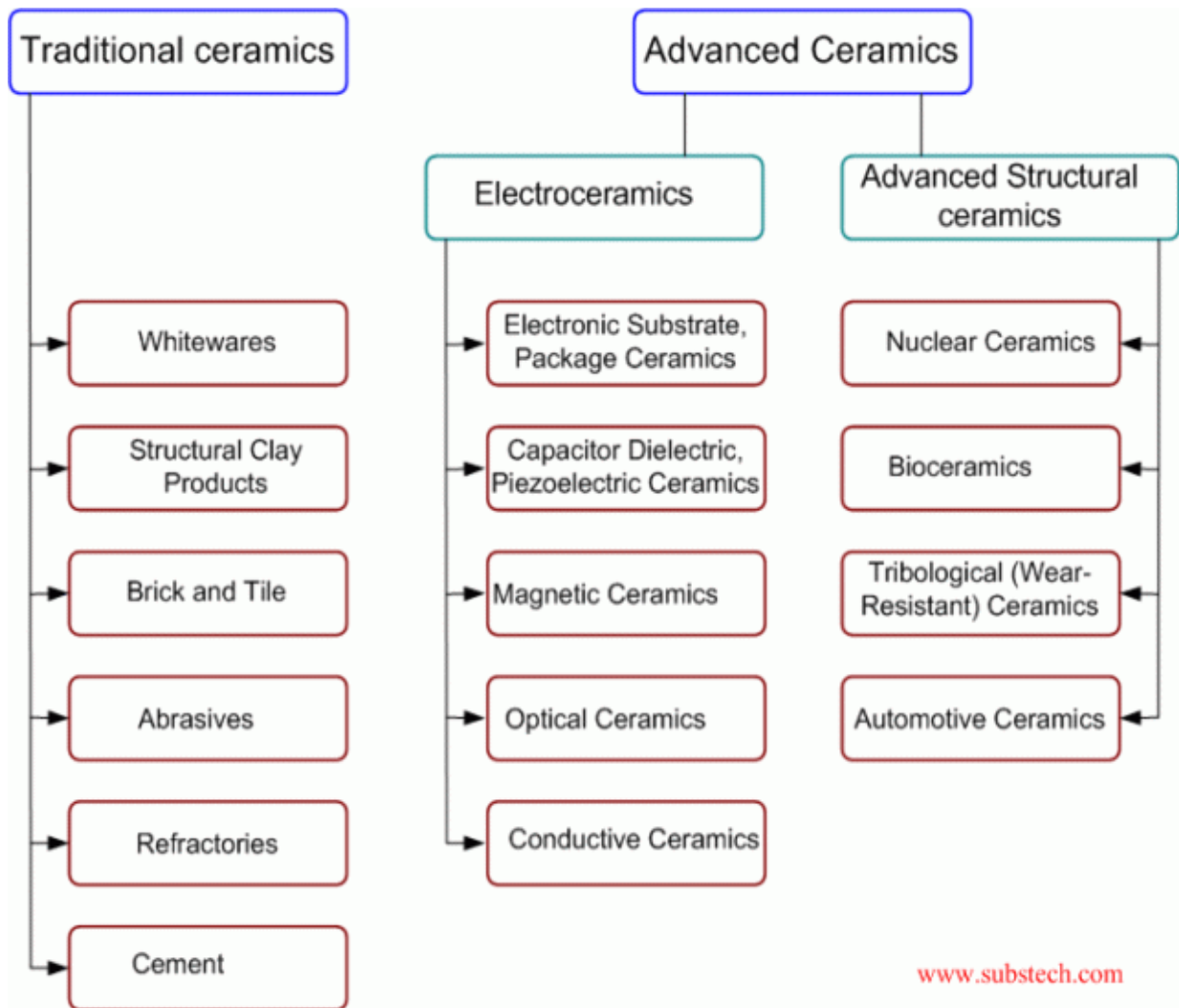


Figure 2.1: General classification of ceramics.

Ceramics can be also classified into:

- Oxide ceramics: include inorganic compounds that are made of a combination of oxygen with another metallic or metalloid element like aluminum (Al), titanium (Ti), silicon (Si), magnesium (Mg) and zirconium (Zr). This type of ceramics could be traditional such as porcelain, or advanced such as Alumina.

- Non-oxide ceramics: they are inorganic ceramics based on compounds of boron, carbon, silicon and nitrogen. They usually contain a high portion of covalent compounds. As a result, they can be used at very high temperature which provides high strength and hardness in addition to the excellent resistance to wear and corrosion. This type of ceramics is advanced such as boron nitride and silicon-carbide. Fig. 2.2 summarizes this classification.

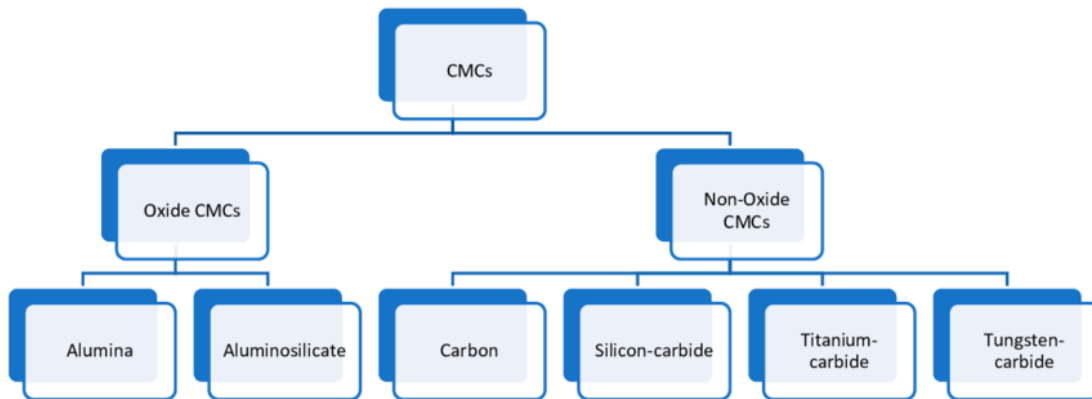


Figure 2.2: Oxide and non-oxide ceramics categories. [14]

2.1.1 Properties of ceramics

Ceramics are compounds made up of two or three elements. For instance, silicon carbide (SiC) is a compound made up of silicon and carbon atoms at most. The atoms in ceramics are attached together by a chemical bond which most commonly can be either covalent or ionic. The properties of ceramic materials are dictated by the atomic scale structure like all materials.

Broadly speaking, most ceramics have the following properties: high melting temperature, non-magnetic, oxidation resistant, chemically stable, thermal insulators durable, prone to thermal shock, hard (strong under compression), brittle (low ductility) and finally, low thermal expansion.

The properties of certain ceramics are shown in Table 2.1. As seen from this table, the melting point for ceramics is relatively high. In addition, we can see that ceramics have low values of Thermal Expansion Coefficient, meaning that they will expand slowly as they are being heated. Knoop Hardness (HK) is used to signify how much a material will resist the indentation of its surface by a hard pyramid probe.

Table 2.1: Properties of some polycrystalline ceramics. [15]

Material	Melting Point (°C)	Thermal Expansion Coefficient ($\times 10^{-6}$ cm/cm)/°C	Knoop Hardness (HK) (100 g)
Al ₂ O ₃	2000	~6.8	2100
BN	2732	0.57 ^a , -0.46 ^b	5000
SiC	2700	~3.7	2500
Diamond		1.02	7000
Mullite	1810	4.5	—
TiO ₂	1840	8.8	—
Cubic ZrO ₂	2700	10.5	—

^aPerpendicular to pressing direction.
^bParallel to pressing direction.

2.1.2 Applications of ceramics

Another way to classify ceramics is based on their functionality. Table 2.2 shows the ceramic categories according to this classification in addition to the related applications as well as some examples of ceramics in each category. For the electrical applications, some ceramics can be used as dielectric materials in capacitors. For example, barium titanate is used for this purpose as it has a high dielectric constant and low dielectric loss. A previous study have proved that the lead free system BT-BLN is a prospective dielectric material to use in pulse power capacitors [16]. Furthermore, an important research would lead to the modification of built-in component dielectric properties contributing in high frequency wireless applications. In that context, a specific kind of inosilicate has been proved to reveal magneto-electric behavior, in which the electric field can influence the electric polarization [17]. In optical applications, an important study has reviewed the latest results done in solid state lasers using (Lu, Sc, Y)₂O₃ ceramic [18]. Another example of mechanical or structural application is using ceramics as cutting tools. Many ceramics can be used for this purpose

such as Al_2O_3 and WC-Co cermets. In addition, many common ceramics are used in construction applications, concrete and glass is a good example in this aspect as they are used in building. Moving to the chemical applications, a recent paper showed that an outstanding efforts in promoting the application of catalysis can be achieved using three dimensional piezoelectric ceramics produced by direct ink writing approach [19]. As for the biomedical applications, ceramics have generally a great potential in dentistry, as discussed in recent study that shows the applications, technologies, fundamentals, experimental techniques, and open issues regarding glass-ceramics in industry [20]. In domestic applications, ceramics play a main role in production of tiles, pottery, whiteware, kitchenware, and jewelry. In automotive applications, perovskite ceramics were fabricated successfully for supported Proton Ceramic Fuel Cells (PCFCs) using thermal inject printing method, which has the advantage of being commercially affordable [21].

Table 2.2: Classification of ceramics based on the main function. [22]

Function	Application	Examples of Ceramics
Electrical	Capacitor dielectrics	BaTiO ₃ , SrTiO ₃ , Ta ₂ O ₅
	Microwave dielectrics	Ba(Mg _{1/3} Ta _{2/3})O ₃ , Ba(Zn _{1/3} Ta _{2/3})O ₃
	Conductive oxides	BaTi ₄ O ₉ , Ba ₂ Ti ₉ O ₂₀ , Zr _x Sn _{1-x} TiO ₄ , Al ₂ O ₃
	Superconductors	In-doped SnO ₂ (<i>ITO</i>) YBa ₂ Cu ₃ O _{7-x} (<i>YBCO</i>)
	Electronic packaging	Al ₂ O ₃
	Insulators	Porcelain
	Solid-oxide fuel cells	ZrO ₂ , LaCrO ₃
	Piezoelectric	Pb(Zr _x Ti _{1-x})O ₃ (<i>PZT</i>), Pb(Mg _{1/3} Nb _{2/3})O ₃
	Electro-optical	<i>PLZT</i> , LiNbO ₃
	Magnetic	Recording media
Ferrofluids, credit cards		Fe ₃ O ₄
Circulators, isolators		Nickel zinc ferrite
Inductors, magnets		Manganese zinc ferrite
Optical	Fiber optics	Doped SiO ₂
	Glasses	SiO ₂ based
	Lasers	Al ₂ O ₃ , yttrium aluminum garnate (<i>YAG</i>)
	Lighting	Al ₂ O ₃ , glasses
Automotive	Oxygen sensors, fuel cells	ZrO ₂
	Catalyst support	Cordierite
	Spark plugs	Al ₂ O ₃
	Tires	SiO ₂
	Windshields/windows	SiO ₂ based glasses
Mechanical/Structural	Cutting tools	WC-Co cermets Silicon-aluminum-oxynitride (<i>Sialon</i>) Al ₂ O ₃
	Composites	SiC, Al ₂ O ₃ , silica glass fibers
	Abrasives	SiC, Al ₂ O ₃ , diamond, BN, ZrSiO ₄
	Implants	Hydroxyapatite
	Dentistry	Porcelain, Al ₂ O ₃
Biomedical	Ultrasound imaging	<i>PZT</i>
	Buildings	Concrete
		Glass
Construction		Sanitaryware
		<i>PZT</i> , B ₄ C
	Defense applications	
	Armor materials	
	Sensors	SnO ₂
Others	Nuclear	UO ₂
		Glasses for waste disposal
	Metals processing	Alumina and silica-based refractories, oxygen sensors, casting molds, etc.
	Catalysis	Various oxides (Al ₂ O ₃ , ZrO ₂ , ZnO, TiO ₂)
	Air, liquid filtration	
Chemical	Sensors	
	Paints, rubber	
	Domestic	
Domestic	Tiles, sanitaryware, whiteware, kitchenware, pottery, art, jewelry	Clay, alumina, and silica-based ceramics, glass-ceramics, diamond, ruby, cubic zirconia, and other crystals

2.1.3 Pyrochlore ceramics

Pyrochlores are functional crystalline solids that have a certain structure with a general formula of $A_2B_2O_7$. In this formula, A represents a cation of a trivalent rare earth metal with oxidation number of +2 or +3, B represents a cation of tetravalent transition metal element with an oxidation number of +4 or +5, and O is Oxygen. The space group of pyrochlores is $Fd-3m$ (227) which is generally characterized by a Face-Centered Cubic (FCC) lattice with 8 units per unit cell as shown in Figure 2.3.

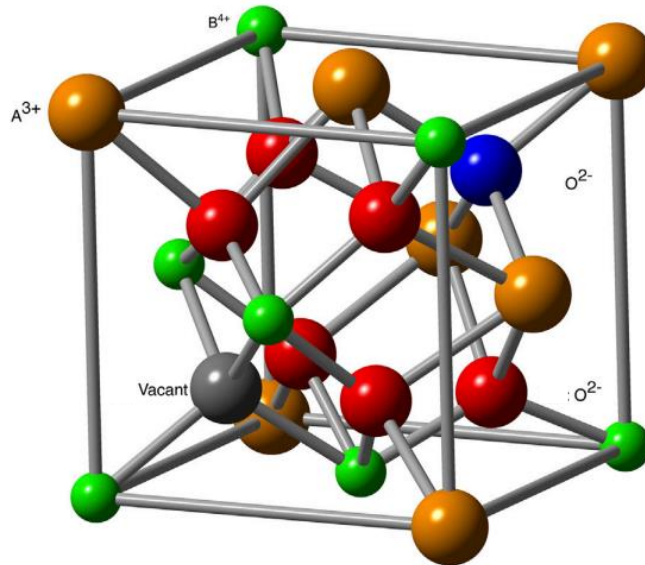


Figure 2.3: The general structure of $A_2B_2O_7$ pyrochlore. [23]

Pyrochlores have been extensively investigated by material scientists and crystallographers, due to the various substitutions that can be assigned to A & B cations or O anion, giving many compounds that possess the pyrochlore structure.

2.2 X-ray

At the beginning of its discovery, x-ray was the expression given to a highly penetrating ray that emanates when electrons having high energy strike a target made of metal. Now, we understand that x-rays are electromagnetic rays of high frequency produced either when electrons are decelerated, or make transitions in heavy elements between lower energy levels.

In 1895, Wilhelm Röntgen, a German physicist and mechanical engineer discovered x-ray. Following that achievement, he earned Noble Prize in Physics in 1901.

2.2.1 X-ray generation

X-ray is produced via the well-known x-ray tube that includes three primary components:

- The cathode and the anode that are separated from each other by a small distance: when heated, the cathode (filament) emits electrons via thermionic emission through the tube vacuum to the anode (target) which collects them.
- An envelope at which the cathode and the anode are contained. It is usually made of glass. It should maintain a vacuum in order to prevent collisions between electrons and gas molecules.
- High voltage source (30-150) kilovolts that should be maintained between the cathode and the anode in order to accelerate the electrons to high speeds.

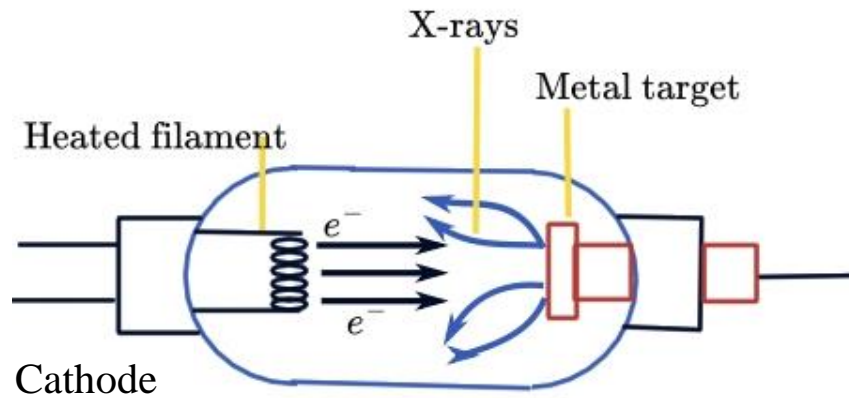


Figure 2.4: Simplified x-ray diagram.

X-rays are produced through the interaction of accelerated electrons with the nuclei of tungsten inside the tube anode. Two kinds of radiation are created:

1. Characteristic X-rays: these rays are emitted when an electron with high energy collides with another electron from the inner shell of target atom. Then, both of them are ejected leaving a hole which is filled by an electron from the outer shell. The energy difference between the two shells is emitted as an x-ray photon. When the hole occurred in the $n=1$ (K-shell), and the outer electron came from the $n=2$ shell, then, the produced x-rays are called K-alpha x-rays. If the outer electron came from $n=3$ shell, the emitted x-rays are called K-beta x-rays. That applies also when holes occurred in L-shell ($n=3 \rightarrow 2$ is L-alpha, $n=4 \rightarrow 2$ is L-beta) and higher main shells ($n=2, 3, 4, 5 \dots$).
2. Bremsstrahlung X-rays: the meaning of Bremsstrahlung is "braking radiation" describing the radiation that is emitted when high energy electrons are braked when they collide with a metal target, usually tungsten. Laws of electrodynamics entails that accelerated charges emit electromagnetic radiation, so when the energy of accelerated electrons is high enough, the radiation will lie in the x-ray regime of the

EM spectrum. It is identified by radiation of continuous distribution that shifts toward high frequencies and becomes more intense as the energy of the fired electrons increases.

Fig. 2.5 shows the main difference between characteristic and Bremsstrahlung x-rays. In Bremsstrahlung x-ray, the resulted x-ray distribution is continuous, whereas in characteristic x-ray, the distribution shows energy values of specific narrow bands.

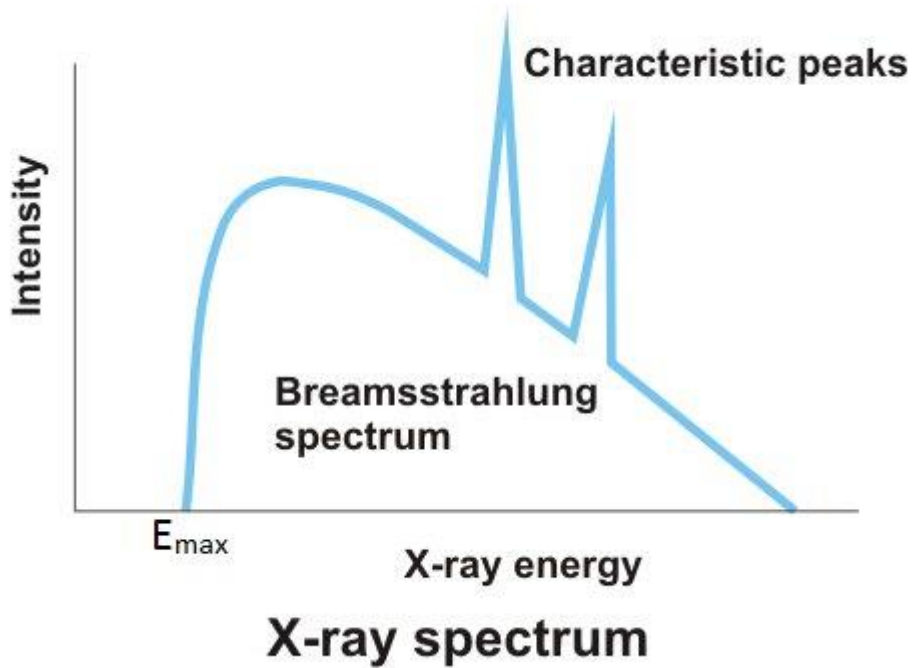


Figure 2.5: Bremsstrahlung vs characteristic x-ray radiation. [24]

2.2.2 X-ray diffraction

Generally speaking, scientists take the advantage of diffraction to study the crystal structure using photons, electrons or neutrons, depending on the wavelength and the crystal structure. The periodicity of lattice in the crystal enables us to benefit from diffraction to study the structure. In our study, we are interested in x-ray diffraction, as its wavelength is smaller or comparable to the distance between crystal planes ($\lambda \leq d$) making it suitable to go

deep and study the crystal structure. X-ray has a wavelength range of (10 nm-10 pm), meaning that it has high energy, which enables it to penetrate materials.

2.2.2.1 Bragg's law

William Henry Bragg and his son, Lawrence Bragg were the first that presented a formulation of x-ray diffraction. In 1915, for their work in determining the crystal structure of diamond, NaCl and ZnS, they were awarded the Nobel Prize in physics.

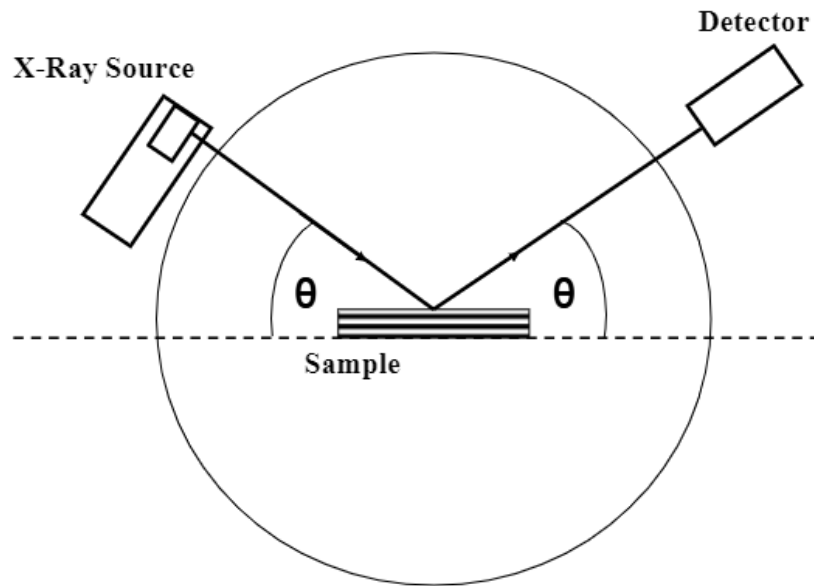


Figure 2.6: Simple schematic diagram of x-ray diffraction. [25]

Bragg's law sheds light on what will happen if an x-ray is incident with an angle θ on the surface of a certain crystal, where it will be reflected with the same scattering angle θ . In addition, a constructive interference occurs when the path difference between beams scattered from different planes equals an integer number of the wavelength will take place in case the path difference is equal to an integer number of the wavelength ($d=n\lambda$).

As a result of Bragg's law, crystal planes reflect x-ray beams at only certain angles of incidence. This condition is usually referred to as Bragg's condition:

$$2d \sin\theta = n\lambda \quad (1)$$

Where λ is the wavelength of incident x-ray, d is the distance between crystal planes, θ is the angle of incidence and n is an integer number.

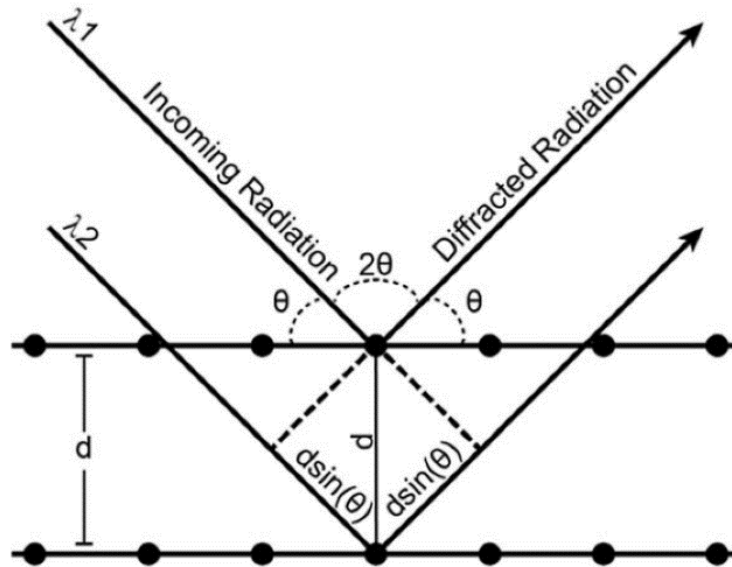


Figure 2.7: Schematic diagram of Bragg's law. [26]

To summarize, the most important points about Bragg's equation are the following:

1. The reflection is specular, meaning that the angle of incidence and the angle of reflection are equal ($\theta_i = \theta_r$).
2. As mentioned above, the path difference must be equal to an integer number of x-ray wavelengths.

Bragg's equation can be used either to know the distance between crystal planes or to specify the wavelength of the applied x-ray when a material with a crystal structure is already known.

2.2.2.2 X-ray powder diffraction

X-ray powder diffraction is a technique used in material science that employs x-rays mainly to investigate the crystal structure of a certain powder material. Other applications for this technique are the following: crystalline materials characterization, unit cell dimensions determinations, purity measurement of a certain sample, quantitative analysis (minerals amounts), fine-grained minerals identification, dislocation density determination, and stress & strain determination of the lattice. Taking CdS as an example for the XRPD pattern shown in Fig. 2.8. Wurtzite is the most stable structure of CdS crystal. The figure shows a simulated XRD pattern for 1 μm bulk CdS. (100), (002), and (101) planes are represented by the first three peaks shown in the figure. It can be noticed that the peak corresponding to the (101) plane is the main peak in the pattern revealing the maximum intensity.

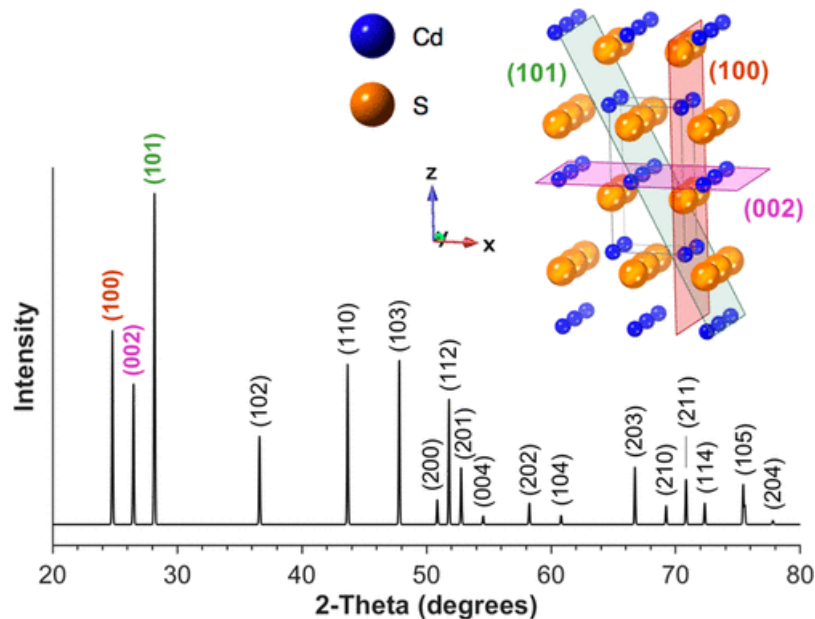


Figure 2.8: Simulated and indexed powder X-ray diffraction pattern for bulk (1 μm) wurtzite CdS. The inset shows the crystal structure of wurtzite CdS with the (100), (002), and (101) planes highlighted. [27]

2.2.2.3 XRD parameters

There are many parameters that can be extracted and investigated using x-ray diffraction technique. In this section, the most important parameters are discussed:

A. Structure factor F_{hkl}

This factor represents a mathematical tool that describes the phase and amplitude of diffracted beam from a crystal plane that is identified using what are known as Miller indices h, k, l .

When there are N atoms in a unit cell, then the total amplitude of the X-rays scattered by the cell is described by the structure factor F , which is the sum of the atomic scattering factors f of the individual N atoms, taking their phases into account:

$$F_{hkl} = \sum_1^N f_n e^{2\pi i(hu_n + kv_n + lw_n)} \quad (2)$$

Where h, k, l are Miller indices of the reflecting lattice planes and u_n, v_n, w_n are the coordinates of the atoms in fractions of the particular edge lengths of the unit cell.

B. X-ray peak broadening

X-ray peak broadening results when lattice is highly distorted or if the crystallite size become less than one micrometer. Both of these two cases restrict the reflection planes number, and since diffraction peaks are due to the constructive interference of reflected x-ray from crystal planes, these two cases will give a wide diffraction peaks. When crystallite size is considerable, we will have a large number of reflection planes and the diffraction peaks will be sharp and narrow. Peaks broadening (β) can also be explained by Scherrer equation mentioned in part C.

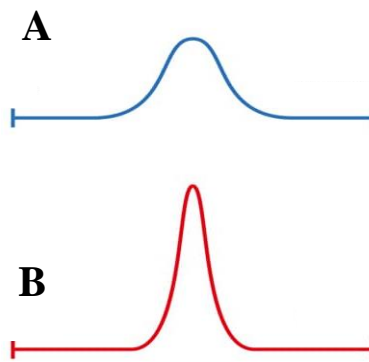


Figure 2.9: A. Broad peak and B. narrow peak.

Steps to calculate the Full Width at Half Maximum (FWHM) that represents the peak broadening are shown in Fig. 2.10 below. FWHM can be eventually calculated by:

$$\beta = \frac{1}{2} (2\theta_{\max} - 2\theta_{\min}) \quad (3)$$

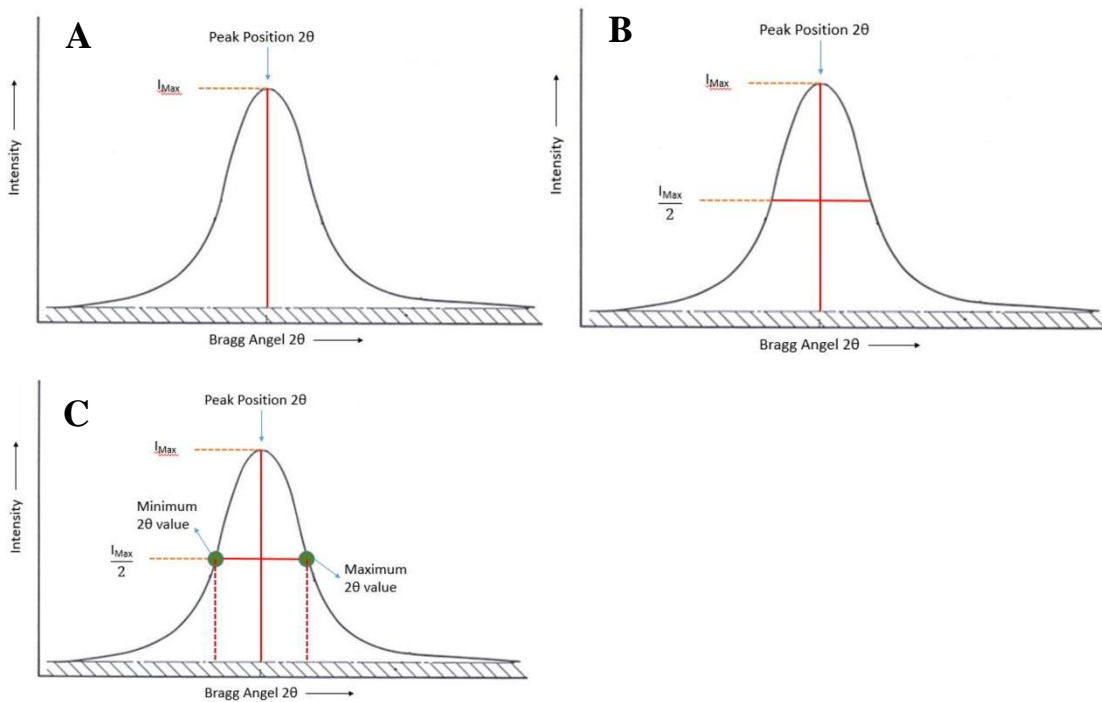


Figure 2.10: Steps of calculating the FWHM from an XRD pattern: A. Some peak at the max. intensity with specific 2θ , B. Illustration of $1/2$ the max. peak intensity and C. Illustration of min. 2θ value and the max 2θ value at $1/2$ the max. intensity. [28]

C. Grain size

The grain is defined as a small region that has a continuous and specific orientation in the crystal lattice. The crystalline solid can be single crystal or polycrystalline. Polycrystalline solids consist of single crystals with different orientations called grains separated by grain boundaries. Hence, each grain in the polycrystalline material can be called a single crystal. The interface between two grains is called the grain boundary which is considered as a two dimensional defect in the crystal structure. As the number of grain boundaries increases, the resistance to dislocation increases. The grain and grain boundary are illustrated in Fig. 2.11 below. When the grain size is finer, that entails more grain boundaries making the material less ductile.

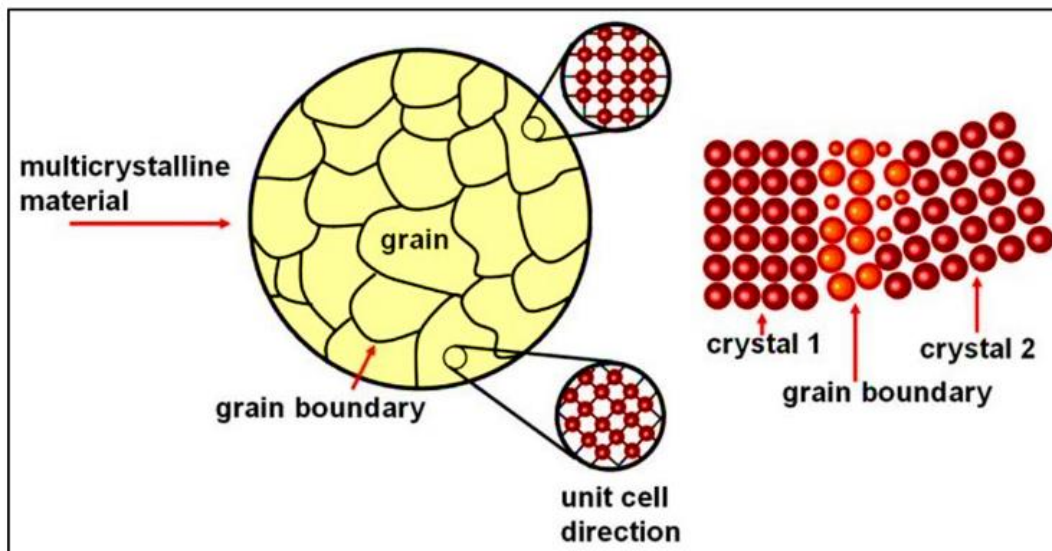


Figure 2.11: Grain boundaries (black) and grains (yellow) in a polycrystal. [29]

Scherrer equation is used to calculate the grain size of a crystal based on the broadening of diffraction peak in XRD pattern. The Scherrer equation is:

$$D = \frac{K\lambda}{\beta \cos\theta} \quad (4)$$

Where D is the crystallite size in nm, it can be equal to or smaller than the grain size, K is the shape factor (0.94), λ is x-rays wavelength, β is FWHM and θ is the diffraction angle in radians.

D. Dislocation density

Dislocation density is defined as the number of dislocations per in unit volume of crystalline material. Its importance arises from influencing the distribution of the grain size. For a point defect, the dislocation density is given by:

$$\delta = \frac{1}{D^2} \quad (5)$$

For a line defect, the formula is:

$$\delta = \frac{15\varepsilon}{aD} \quad (6)$$

Where in both equation (5) and equation (6), δ represents the dislocation density measured in units of $n^{-1}m^{-2}$. D is the crystallite size from Scherrer equation, a is the lattice constant and ε is the strain. The dislocation density can be obtained from an XRD pattern after calculating the crystallite size from equations (5) & (6).

E. Stacking faults (SFs)

Stacking faults are crystallographic planer defects taking place in crystalline materials, deviating from the periodic patterns of atoms layers in the crystalline structure. These faults can arise from translation between subsequent two planes, insertion of a wrong layer through the sequence or a change in the sequence of a certain layer. They can arise from either plastic deformation or during the growth of the crystal. They differ also from dislocations in that they represent planer defects, whereas dislocations represent point or linear defects.

The most famous example of stacking faults can be found in the close-packed structures. It's known that the Face Centered Cubic (FCC) structures differ from the Hexagonal Close Packed (HCP) structures in stacking order only. This difference is shown in Fig. 2.12. Both of the two structures are close packed having six-fold symmetry, the atoms take shape of equilateral triangles. When we arrange a layer on top of another, the atoms are not directly aligned above each other. It can be noticed that the two first layers are the same for the FCC

& HCP and marked AB. The third layer is the separator difference between the two structures, if the atoms of this layer are aligned directly above the atoms of the first one, then stacking will be ABA, giving the HCP structure which continues as (ABABAB...). For stacking in the [111] direction of the FCC structure, atoms in the fourth layer are placed directly above those in the first layer producing a stacking of (ABCABCABCABC...).

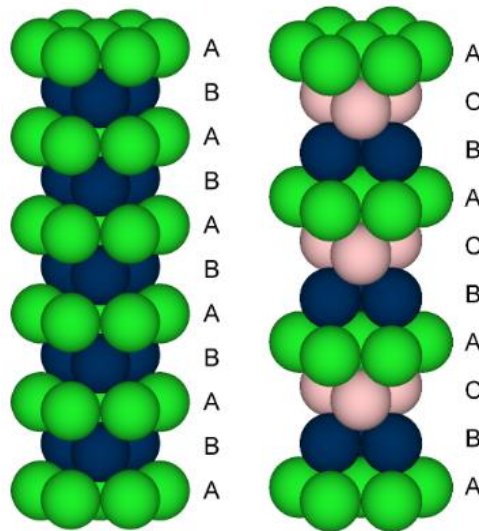


Figure 2.12: FCC (right) vs HCP (left) structure. [30]

Peaks arising or missing in the XRD patterns, deviating from those found in the common one, are sometimes due to the presence of stacking faults in the sample.

F. Stress and strain

Strain and stress are two important and common concepts in material science. Generally speaking, stress is defined as the force applied to a certain material per unit area, while strain is the change in the shape of that material resulting from that applied force. Stress and strain can be useful in studying the properties of materials, which help in determining the most suitable material to a certain application.

Strain can be found from an XRD pattern by:

$$\text{strain} = \varepsilon = \frac{\beta}{4\tan\theta} \quad (7)$$

Where β is the FWHM and θ is the diffraction angle in radians.

An important equation that relates the x-ray peak broadening, crystallite size and strain together is the combined formula of Stokes-Wilson and Scherrer equation given by:

$$\beta \cos \theta = \frac{0.94\lambda}{D} + \varepsilon \sin \theta \quad (8)$$

Where β is the FWHM, λ is x-rays wavelength, D is the crystallite size, ε is the strain and θ is the diffraction angle in radians.

G. Thermal Expansion Coefficient (TEC)

Thermal expansion coefficient is the rate at which materials expand with increasing temperature, usually determined under constant pressure. Generally speaking, it is known that ceramics have extremely low values for TEC in contrast to polymers which have very high TEC values. The change of size with varying temperature can be a change in volume, area or length. In temperature dependent XRPD patterns, TEC can be calculated from the following equation:

$$\alpha = \frac{\Delta a}{a} \left(\frac{1}{\Delta T} \right) \quad (9)$$

Where α is the Thermal Expansion Coefficient measured in $\frac{1}{C}$, Δa is the change in lattice constant and ΔT is the change in temperature.

2.3 Synchrotron light source

A synchrotron consists of a particles accelerator (typically electrons) that gives an intense beam of light with intensities and wavelengths which allow the study of objects in details. The size of these objects ranges from human cells down to atoms. Synchrotron light source is an Electromagnetic radiation (EM) source produced using a storage ring mainly for technical and scientific purposes. In recent days, the exceptional power of synchrotron

has a major impact in many fields including: chemistry, physics, biology, material science, medicine, geology and archaeology.

2.3.1 A general glimpse about synchrotron facilities

The first synchrotron was built in 1946 and was dedicated to study collisions between very high energy particles. Nowadays, approximately, there are 70 synchrotrons around the world at different development stages (operational or under construction).



Figure 2.13: A scheme of synchrotron facility. Copyright © EPSIM 3D/JF Santarelli, Synchrotron Soleil.

Two examples of constructed synchrotrons are:

- ANSTO's, which is a 3 GeV Australian synchrotron with 10 beamlines that supports a wide range of research in many fields such as nanotechnology, medicine and manufacturing.



Figure 2.14: ANSTO's facility. [31]

- SESAME (Synchrotron-light for Experimental Science and Applications in the Middle East), which is a 2.5 GeV synchrotron with 5 operational beamlines.



Figure 2.15: SESAME facility. [32]

Since they are very large facilities, synchrotrons are extremely expensive and the access to them is very limited. For this reason, they are mostly constructed by international collaboration like in case of SESAME.

2.3.2 Synchrotron light properties

The most important properties of synchrotron light are the following:

- High brightness: synchrotron light is highly intense.
- The resulted light is pure since it is produced at an ultra-high vacuum.
- Continuous light: meaning that light stays on constantly.
- Synchrotron light is emitted in very short pulses, typically, less than one nano-second, which enables time-resolved researches.
- High collimation: since the accelerated electrons have a relativistic speeds, the produced radiation is highly collimated, meaning that the rays in the beam are parallel to each other.
- Wide energy range: the energies of emitted synchrotron light range from infrared (IR) light to the region of hard x-ray as shown in Fig 2.16.

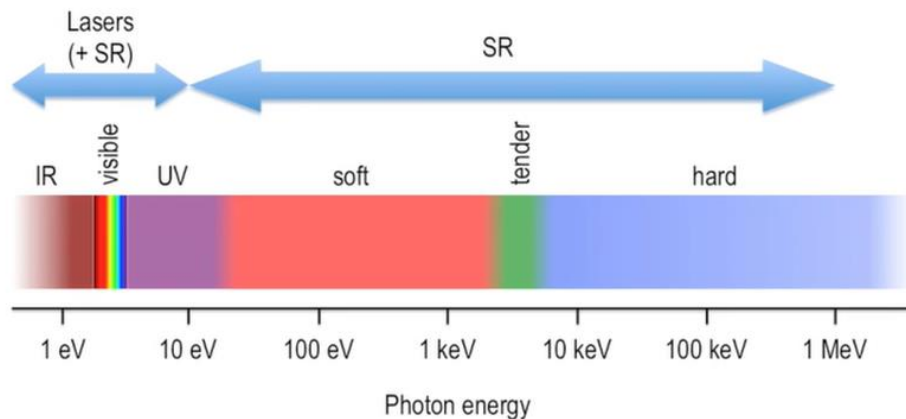


Figure 2.16: Synchrotron rang on the EM spectrum.

- Highly polarized: the polarized radiation emitted by synchrotron can be linear, circular or elliptical.
- Tunable: an intense beam with any selected wavelength can be obtained.

Compared to the conventional XRD technique, synchrotron facilities give the user greater possibilities. Many cases require to choose synchrotron sources to study the samples: for example, in many experiments, it is required to probe the samples deeply at which very high photons energy are needed. Also, synchrotron sources provide an intense flux enabling the researcher to measure materials of small volume. Another case is that some experiments entail special environments such as furnace of high temperature.

2.3.3 Synchrotron machine at SESAME

In this section, synchrotron facility specifications and properties at SESAME where the samples where studied are discussed in details.

Synchrotron facility at SESAME has five main components:

1. LINAC: generally speaking, electrons generated via thermionic emission from hot element in an electron gun. Through a linear accelerator (LINAC) (shown in Fig. 2.17), electrons are accelerated to about 100-MeV. A regular electrons supply is needed since electrons are being lost in this machine due to the existence of residual gas particles in the storage ring.

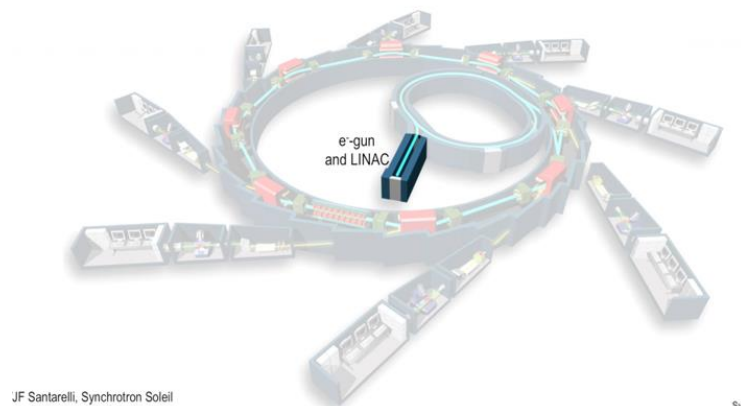


Figure 2.17: LINAC & e-gun. Copyright © EPSIM 3D/JF Santarelli, Synchrotron

In case of SESAME, classical Microtron emits and accelerates electrons up to 20-MeV as needed. LaB6 crystal is needed to extract electrons through a 4- μ s long & 63-KV magnitude voltage pulse. Then, electrons are injected into a 3GHz RF cavity that accelerates them at a rate of approximately 0.535 MeV in each turn using a 4- μ s long & 45-kV magnitude RF pulse. The 20-MeV electrons are extracted using a deflection tube from the Microtron. Finally, they are transferred through the transfer line (TL1) to the booster.

2. **Booster ring:** it is called so since the electrons get an energy boost on each turn. After being accelerated by LINAC, electrons are injected into the booster ring (shown in Fig. 2.18) at which they were accelerate. After that, they are being injected into the storage ring periodically at which they circulate for hours.



Figure 2.18: The booster ring. Copyright © EPSIM 3D/JF Santarelli, Synchrotron

The booster ring has 38.4 m circumference and is composed of six similar FODO (F-Focusing Quadrupole, D-Defocusing Quadrupole, O-drift space) cells, which contain two Bending magnets (BM), one Defocusing Quadrupole (QD) and two Focusing Quadrupoles (QF) in each, in addition to one horizontal corrector and one beam position monitor in each straight section. Electrons are extracted at 800-MeV after being injected into the booster at

20-MeV. Finally, electrons are transferred to the storage ring via the transfer line (TL2). The accelerating RF system has a frequency of 500-MHz.

3. Storage ring: A ring of magnets is the heart of synchrotron light source as shown in Fig. 2.19.

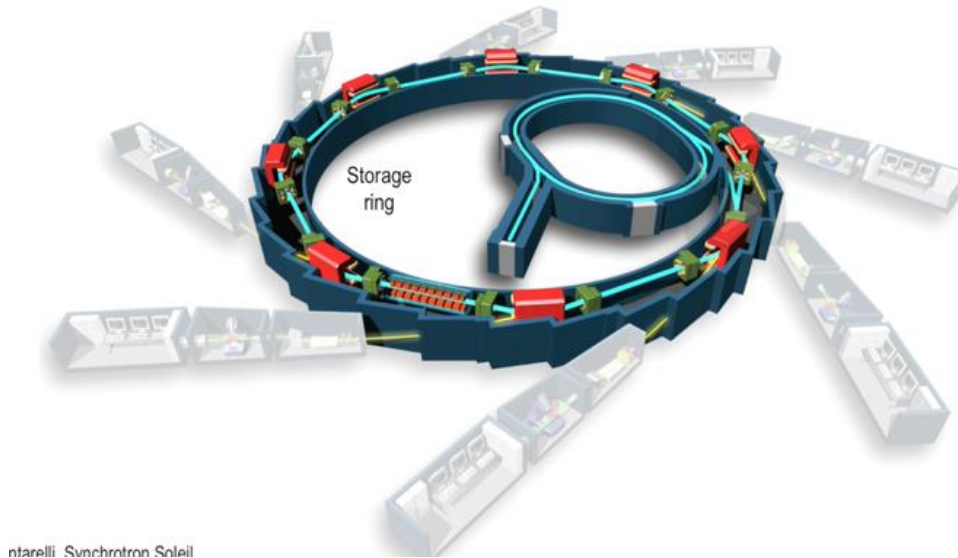


Figure 2.19: The storage ring. Copyright © EPSIM 3D/JF Santarelli, Synchrotron

The structure of this heart contains the following:

- a) Bending magnets (BMs): which represent the arced sections of the storage ring. Through using this array of magnets (which very often referred to as the magnet lattice of the storage ring), this part contains the electrons and preserve them on a closed path. The electrons have relativistic velocities (only slightly lower than speed of light) and their kinetic energies are measured in GeV. These magnets are generally of three types:
 - Dipole (bending) magnets: maintains a closed orbit of electrons through causing the electrons to deflect from their path (electron beam bending).
 - Quadrupole magnets: used for focusing the divergent electron beam.

- Sextupole magnets: used for controlling the chromatic aberration results from focusing by quadrupoles.

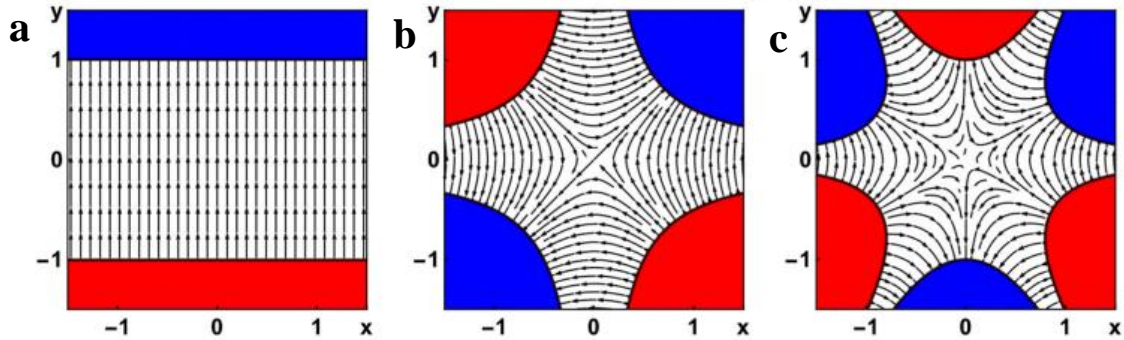


Figure 2.20: each type: a. dipole, b. quadrupole and c. sextupole shows poles & streamlines of magnetic field in transverse cross section. South (-ve electrostatic potential) & north (+ve electrostatic potential) poles are shown in blue and red. [33]

Forcing the electrons to follow a curved path causes the emission of the electromagnetic radiation (as entailed by electrodynamics laws for accelerating electrons charges) which is the synchrotron radiation. BMs of the storage ring are shown in Fig. 2.21 below.

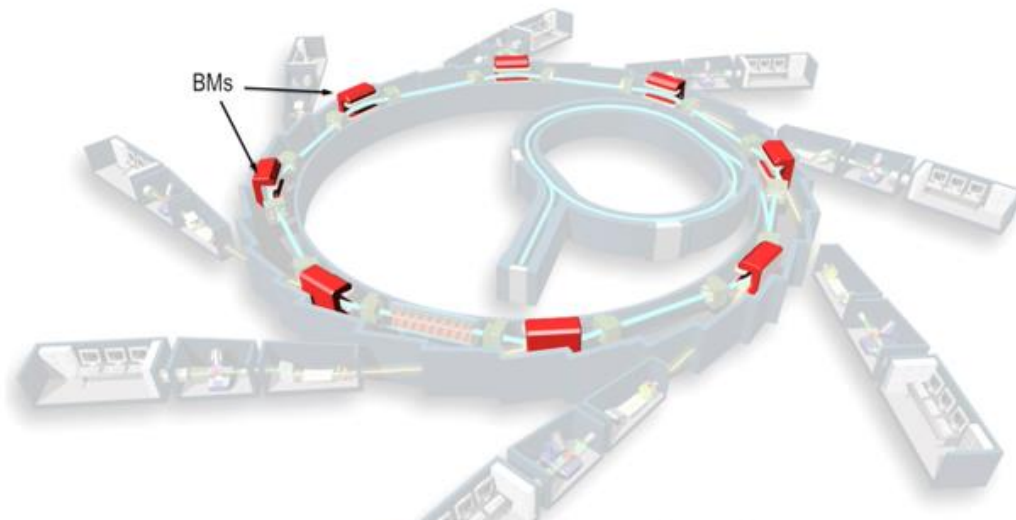


Figure 2.21: The bending magnets of the storage ring. Copyright © EPSIM 3D/JF Santarelli, Synchrotron Soleil.

Fig. 2.22 shows pictures of the three types of the bending magnets at SESAME's storage ring.

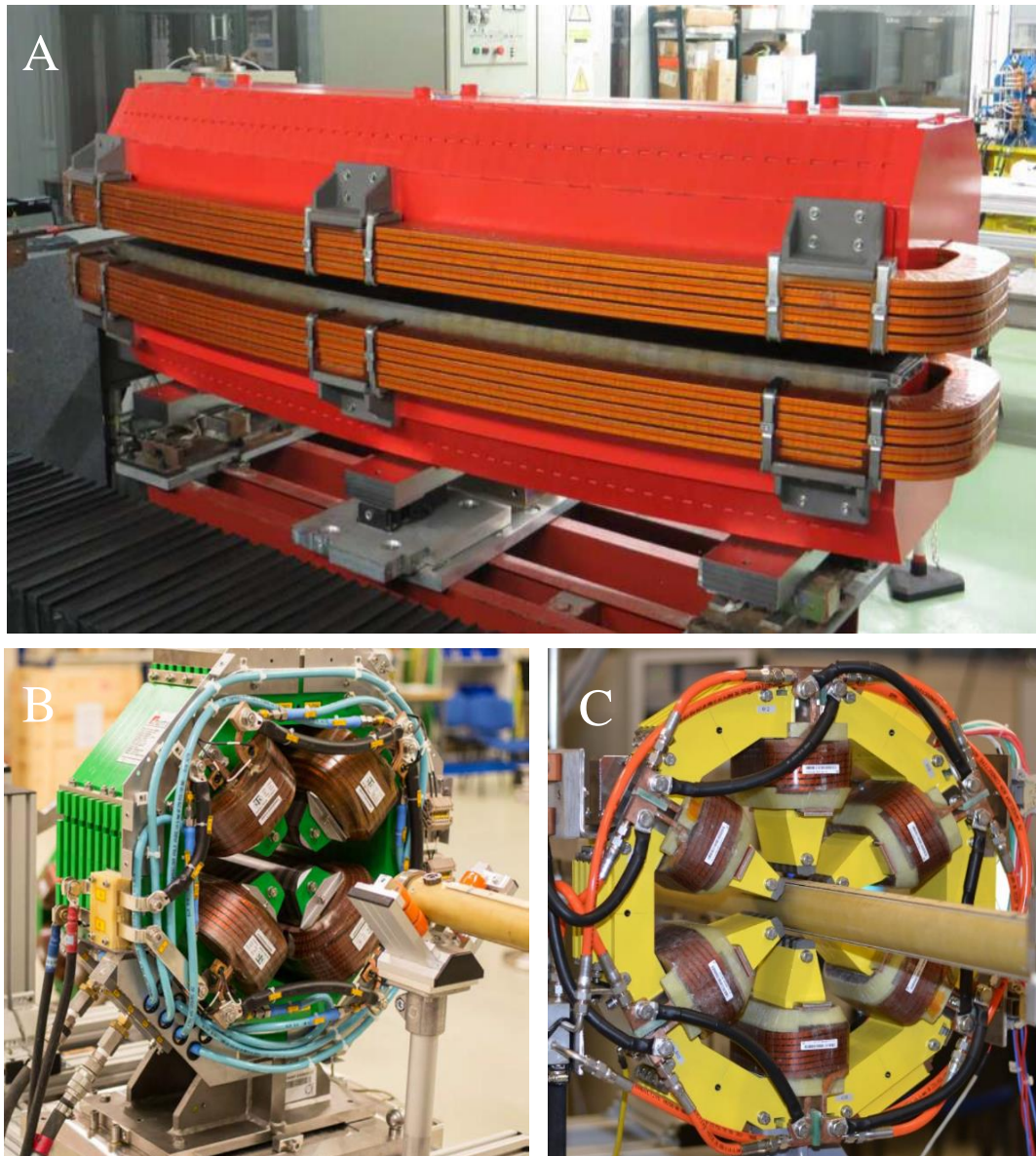


Figure 2.22: A. dipole, the first type of bending magnets in the storage ring. B. the second type, Quadrupole, C. the third type, Sextupole. In the storage at SESAME, there are 16 dipoles, 64 Quadrupoles and 64 Sextupoles. [32]

- b) Insertion devices (IDs): which are the straight sections that lie between BMs. They represent an alternating arrays of North South, South-North dipole pairs as shown in Fig. 2.23.

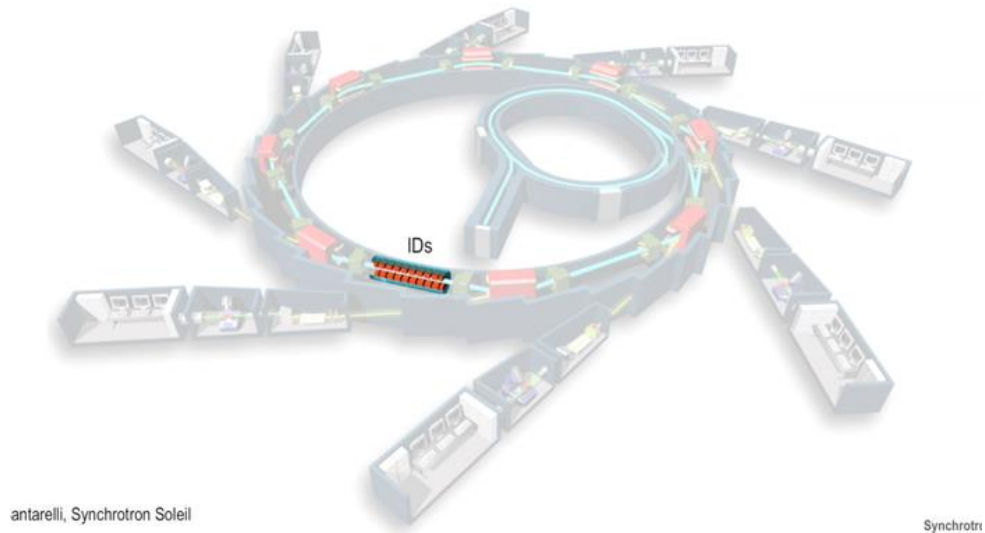


Figure 2.23: Insertion devices (IDs). Copyright © EPSIM 3D/JF Santarelli, Synchrotron Soleil.

Insertion Devices force electrons to move in an oscillatory track in the storage ring plane. That is possible using dipoles set producing alternative magnetic field. Insertion devices are divided into wigglers and undulators.

The heart of the storage ring has a 133.2 m circumference and an energy of 2.5 GeV. After being accelerated to a very high energy, electrons are stored in this heart. Then, these electrons emit the synchrotron light that is directed across the beamlines which are connected to the storage ring and surround it. Every beamline is constructed for a certain type of research. The maximum capacity of the storage ring is 25 beamlines. It is filled with electrons at 800 MeV with a repetition rate of 1 Hz. The magnet lattice of the storage ring is 8-fold one and is a simple DBA (Double Bend Achromat) from which each cell composed of Bending Magnet of combined function surrounded by 2 QF (Focusing Quadrupoles), 2

QD (Defocusing Quadrupoles), 2 SF (Focusing Sextupoles) and 2 SD (Defocusing Sextupoles).



Figure 2.24: part of the storage ring at SESAME including BMs & IDs.

[32]

4. Radio frequency (RF) cavity: The radio frequency system is used to provide electrons with an extra energy once they reach and pass through it to compensate for the energy that electrons lose as a result of synchrotron radiation emission. Radio-Frequency system accelerates electrons using the component of the electric field in the microwave (using alternative voltage), in order to keep up with the operational energy of SESAME at 2.5 GeV.

At SESAME, the RF system operational frequency is 3 GHz in the Microtron & 500 MHz in the storage ring and the booster. The number of cavities is one in the booster and four in the storage ring. All are shown in Fig. 2.25.

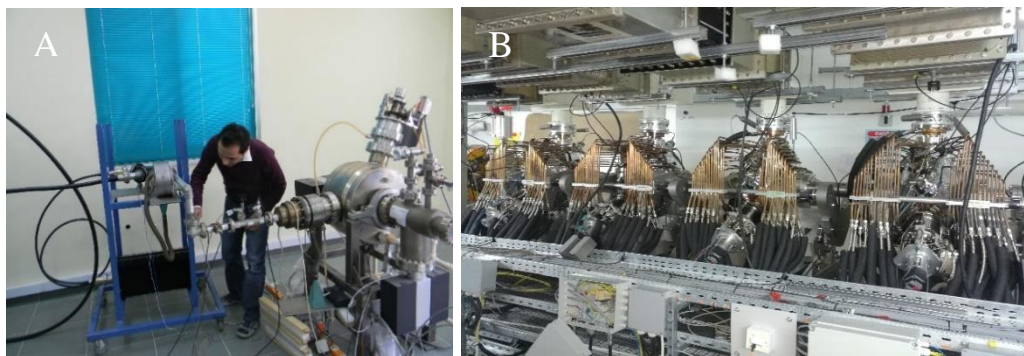


Figure 2.25: RF system at SESAME in: A. the booster ring and B. the storage ring. [32]

5. Beamlines: As mentioned earlier, electrons in the synchrotron emit the intense synchrotron light as they circulate at a speed near the speed of light and their path being bent by the bending magnets. The emitted light is collected by the beamlines that are connected to the storage ring. Each beamline contains optical elements that focus certain wavelengths of synchrotron light on different materials under study. Each beamline produces light with characteristics that are suitable for a certain research type. The beamlines are the physical areas in the experimental hall where the users conduct their experiments.

At SESAME, there are eight beamlines, we are interested in the beamline we worked inside which is the Material Science beamline so we will talk only about it in this chapter.

The Materials Science-X-ray Powder Diffraction (MS/XPD) beamline at SESAME is shown in Figure 2.26. It is based on components installed previously Swiss Light Source (SLS). This beamline is used for XRPD (X-ray Powder Diffraction) applications. Its optical design covers an energy range of (5-25) KeV. At this beamline, XRPD technique can be applied for (quantitative analysis, material phase identification, atomic structural determinationsetc.).

The prime components of the front end for this beamline are: fixed mask that is important to define the acceptance angles of the beamline, photon shutter for stopping the beam of photons when necessary, rotating filter, white beam slits and radiation stopper.



Figure 2.26: The Materials Science-X-ray Powder Diffraction (MS/XPD) beamline at SESAME.

Chapter Three: Experimental Details

The experimental details in our research have mainly two essential steps: preparation of BZN pyrochlore samples doped with Cr, Ni and studying the samples at the material science-X ray powder diffraction beamline. The details of the two steps are provided in the following two sections:

3.1 Doped $\text{Bi}_{1.5}\text{Zn}_{0.92}\text{Nb}_{1.5}\text{O}_{6.92}$ Ceramics Preparation

The traditional solid-state route (or sometimes called ceramic method) is very often used in the formation of well-defined crystalline bulk materials. That is possible through causing a chemical reaction by starting with solid materials as carbonates or oxides to form a new one. A high temperature is employed for the reaction to occur since constituent elements do not react at RT. Large scale production and simplicity are advantages of this route. This method generally have the following sequential main steps:

- A. Selection of the starting solid materials: this depends on the expected nature of the resulted material.
- B. Weighing.
- C. Mixing: after the solids have been weighed out in proper amounts, they are then mixed. Usually, a mortar and a pestle are used. An enough amount of certain volatile organic liquid such as alcohol or acetone is added to the mixture to achieve homogenization. The previous steps form a paste. During mixing process, the organic liquid usually evaporates completely after (10-15) minutes. An important consideration for the container is that it should be chemically inert so it does not react with the sample. Ball milling shown in Fig. 3.1 can be used also in the mixing step. It uses a rotating cylinder filled with a small ceramic balls or metal balls to refine

and mix powders. The balls then dropped, grinding the needed material into fine powders that have a uniform size of particle.

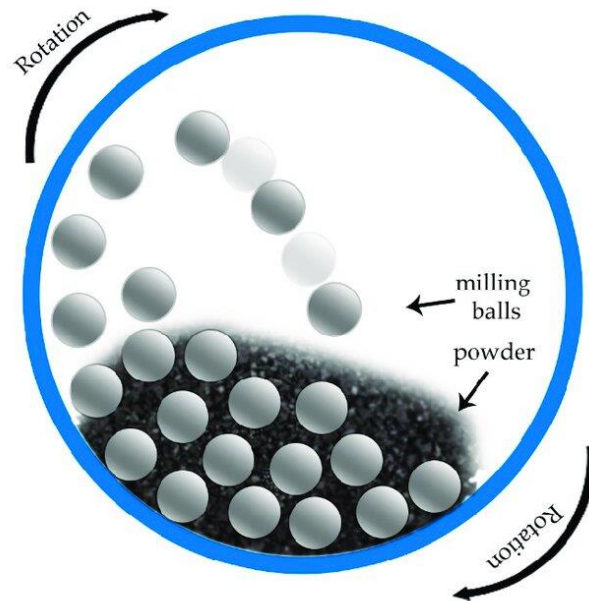


Figure 3.1: Ball milling method for mixing. [34]

- D. Drying: in this step, a hot plate or an oven is needed to expel the water from the material or reduce the moisture content.
- E. Calcination: it is different from drying in that it requires a high temperature so a furnace is used, and the result is a powdery form.
- F. Re-milling.
- G. Pressing or pelletizing: which is the process of compressing the material into a pellet shape.
- H. Sintering: a treatment under high temperature to fuse particles without complete melting. Bridges form between the particles as a result of atoms diffusion to the points of contact. Any remaining voids will be filled by further diffusion. In sintering process, the driving force is the reduction of the total area of surface for the powder particles.

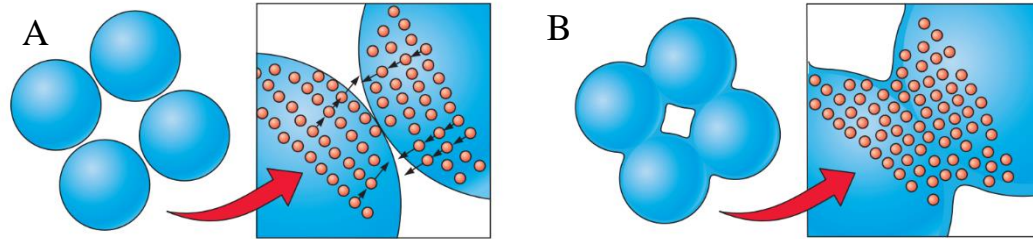


Figure 3.2: A. Compacted product, B. Partly sintered product. [35]

Eight samples are studied in the experiment:

I. Cr doped BZN (with $x=0.10$ & $x=0.06$)

Cr doped BZN pyrochlore ceramics were prepared by solid state mixing of oxides. Knowing that the composition for the powder samples is $\text{Bi}_{1.5}\text{Zn}_{0.92}\text{Nb}_{1.5-x}\text{Cr}_x\text{O}_{6.92-x}$, the main steps of the method are as follows:

Firstly, they were prepared by the use of the following oxides which were weighed in proper ratios: Bi_2O_3 (99.99%, Aldrich), Nb_2O_5 (99.5%, Merck), ZnO (99.5%, Aldrich) and Cr_2O_3 (99%, Alfa Aesar), then, the oxides were mixed with ethyl alcohol in a polyethylene container using milling media of zirconia for 15 hours. After mixing process, the mixed powders were dried and calcined for four hours at $800\text{ }^\circ\text{C}$, then, re-milling is performed. The mixed powders were pressed into pellets shown in Fig. 3.3 below, having a diameter of 10 mm and a thickness of 2 mm.

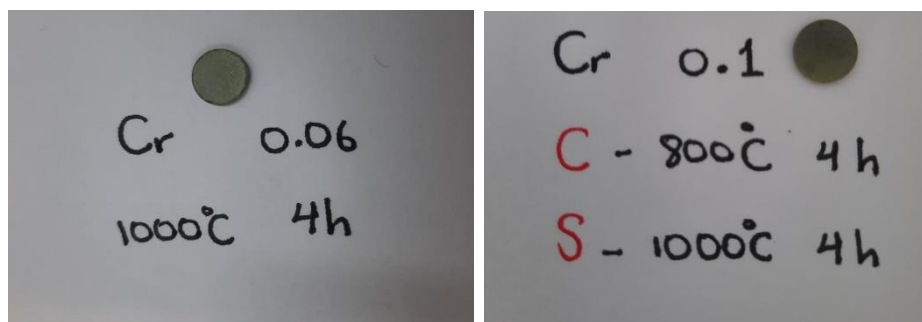


Figure 3.3: Cr doped BZN samples attached with Sintering and calcination temperatures.

After that, the samples were sintered at 1000 °C for four hours in air and in a closed alumina crucible to prevent any evaporation losses. Finally, the samples were crushed using mortar and pestle shown in Fig. 3.4 into fine powders.



Figure 3.4: Mortar and pestle to crush ceramics pellets into fine powder.

II. In doped BZN (with $x=0.05$, $x=0.08$ & $x=0.1$)

In doped BZN pyrochlore ceramics were prepared by the conventional solid state mixing of oxides. Knowing that the composition for the powder samples is $\text{Bi}_{1.5}\text{Zn}_{0.92-3x/2}\text{In}_x\text{Nb}_{1.5}\text{O}_{6.92}$, the main steps are very similar with the previous samples, so just the minor differences will be mentioned.

At first, they were prepared by the use of the following oxides which were weighed in a proper ratios: Bi_2O_3 (99.99%, Acros), Nb_2O_5 Nb_2O_5 (99.5%, Alfa Aesar), ZnO (99.5%, Sigma-Aldrich) and In_2O_3 (99.9%; Alfa Aesar). The powders were pressed into pellets having a diameter of 10 mm and a thickness of (1.0-2.0) mm. The samples were sintered at 1025 C° , 1026 C° & 1050 C° as shown in Fig. 3.5 for four hours in air and in a closed alumina crucible to prevent any evaporation losses.

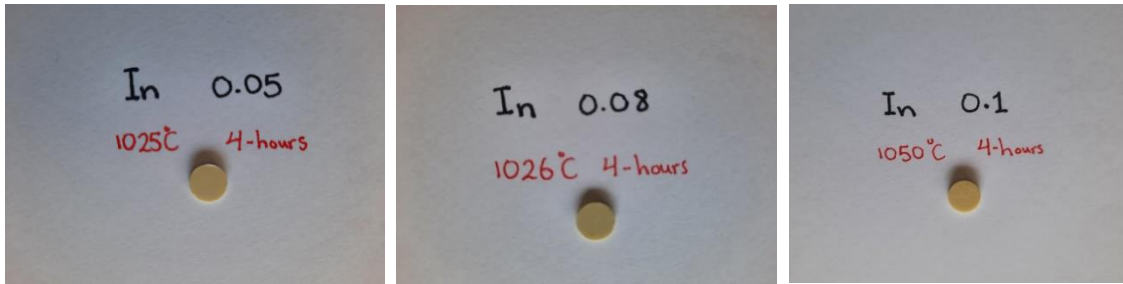


Figure 3.5: In doped BZN samples attached with the sintering temperature.

III. Ni doped BZN (with $x=0.07$, 0.1 & 0.15).

Ni doped BZN pyrochlore ceramics were prepared by the conventional solid state mixing of oxides. Knowing that the composition for the powder samples is $\text{Bi}_{1.5}\text{Zn}_{0.92}\text{Nb}_{1.5-x}\text{Ni}_x\text{O}_{6.92-3x/2}$, again, the main steps is very similar with the previous samples, so just the minor differences will be mentioned.

At the beginning, they were prepared by the use of the following oxides which were weighed in a proper ratios: Bi_2O_3 (99.99%, Aldrich), Nb_2O_5 Nb_2O_5 (99.5%, Merck), ZnO (99.5%,

Aldrich) and NiO. Then, the oxides were mixed and milled inside a polyethylene bottle using ball milling technique in ethanol by zirconia ball for 4 hours. The powders were pressed uniaxially into pellets shown in Fig. 3.6 below, having a diameter of 10 mm and a thickness of (0.5-1.5) mm. The samples were sintered at 1000 °C for four hours in air and in a closed alumina crucible to prevent any evaporation losses.

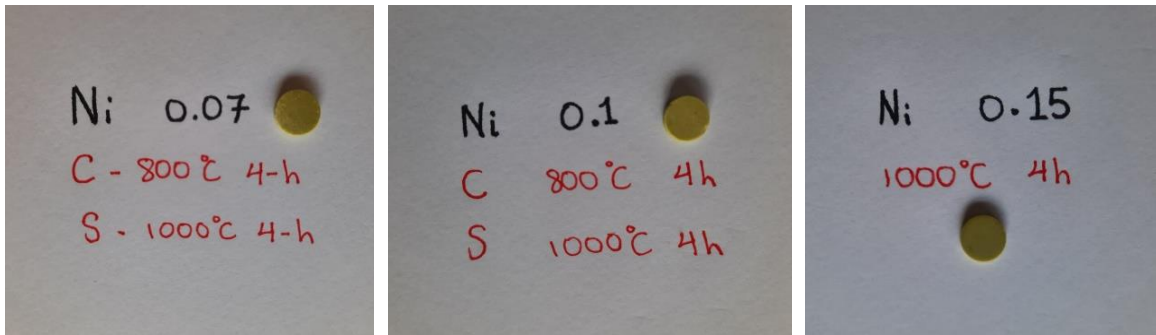


Figure 3.6: Ni doped BZN samples attached with calcination and sintering temperatures.

3.2 Material Science-X Ray Powder Diffraction (MS-XPB) beamline

MS/XPB beamline was used to study the samples, it contains three parts:

- Source:

The beamline depends on a source wiggler that operated at (1.38 T). Comparing to the bending magnet source, the wiggler has a high produced flux.

Generally, the front end of any beamline consists of the components lies in the ring tunnel, directly after either the bending magnet or the insertion device (wiggler in case of MS/XPB beamline). The primary components of the front end at SESAME are:

- ✓ Fixed mask: in order to define the acceptance angles of the beamline.
- ✓ Photon shutter: for stopping the beam of photons when that is necessary.

- ✓ Rotating filter: it might be needed to filter out the soft x-ray region in the source spectrum.
- ✓ White beam slits: for soft x-ray in synchrotron radiation.
- ✓ Radiation stopper: working together with the photon shutter to stop the beam.
- Optical layout

The optical layout of the MS/XPD beamline at SESAME consists of the following components all shown in Fig. 3.7:

- ✓ Collimating mirror that is fixed aligned to 3 meter rad grazing angle.
- ✓ Then, double crystal mono fixed exit monochromator which is located for energy selection.
- ✓ Finally, focusing mirror in order to focus the beam in a vertical way.

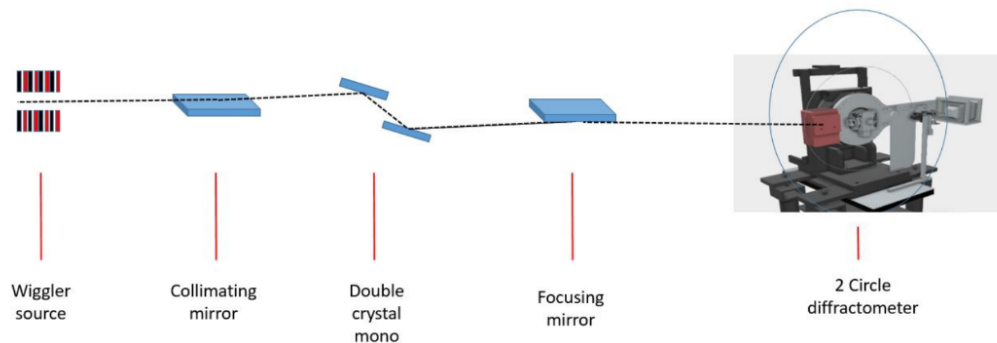


Figure 3.7: the optical layout of the MS/XPD beamline at SESAME. [32]

- Experimental station

The MS/XPD experimental station shown in Fig. 3.8 basically consists of two refurbished circle diffractometer that was previously installed at I19 beamline (at Diamond Synchrotron at UK). There is an inner rotary (θ) for the sample rotation, and another rotary (2θ) for the detector rotation. For transmission experiments, a homemade spinner is fixed on XY translational stage attached to the θ rotary. Heating samples inside capillaries is possible by using a hot gas blower.

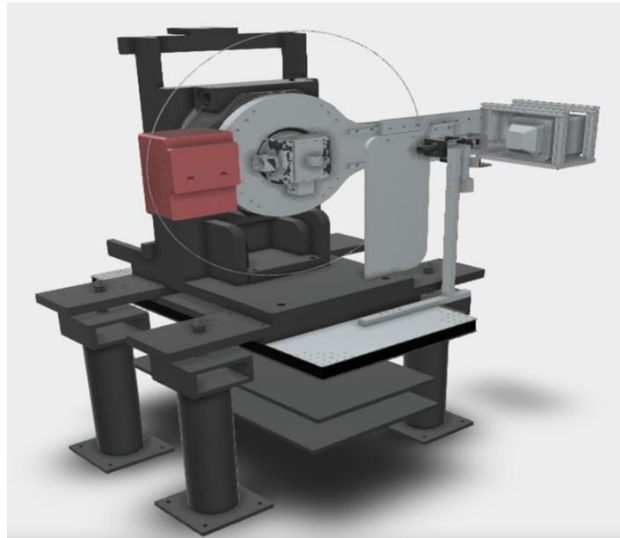


Figure 3.8: the diffractometer used in MS/XPD beamline at SESAME. [32]

Completing our experimental steps at SESAME, after preparing the samples in the powder form, as shown in Table 3.1, we chose two of the samples to be investigated up to 600 °C with a step of 25 °C, which were (0.10) Cr doped BZN & (0.10) Ni doped BZN. The other samples were studied at room temperature.

Table 3.1: The temperatures at which our samples were studied.

Sample	Temperature
(0.10) Cr doped BZN	(50-600) C°
(0.10) Ni doped BZN	(30-600) C°
(0.06) Cr doped BZN	RT
(0.07) Ni doped BZN	RT
(0.15) Ni doped BZN	RT
(0.05) In doped BZN	RT
(0.08) In doped BZN	RT
(0.10) In doped BZN	RT

In the next step, we selected the Quartz for the two samples to be studied up to 600 °C since it is dedicated for temperature dependent studies, the Boro Silicate is for the samples to be studied at room temperatures. They have a diameter of 0.5 mm and we filled them to about 2 cm long. Both of them are shown in Fig. 3.9 below.



Figure 3.9: Quartzkapillaren (the red one) and borokapillaren (the green one).

Then, these capillaries were filled with samples powders, the detailed procedures is as follows: filling the capillary with the sample powder, using the vibrating device shown in Fig. 3.10 to make the grains compact and close to each other as much as possible and cutting off the unnecessary part of the capillary.



Figure 3.10: Electrocautery device (on right) & (vibrator) (on left).

After that, we used the electrocautery shown in Fig. 3.10 to dissolve the wax used to fix the sample and keep it straight up at the capillary spinner as shown in Fig. 3.11.

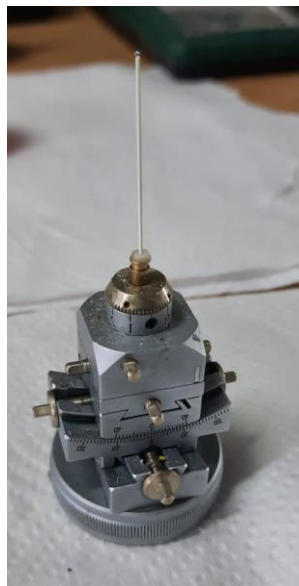


Figure 3.11: the capillary spinner used to fix the sample.

Then, we fix the capillary spinner in its place directly above the gas blower in the diffractometer as shown in Fig. 3.12. The gas blower set up requires nearly one hour, knowing that the gas blower is dedicated for temperature dependent studies (Rt-1000) °C. Finally, we left the experimental room and turned on the device. Regarding the samples to be studied until 600 °C, the total time required for one sample is 465 min -eight hours- divided into: heating time: 115 min, exposure time: 230 min, cooling time: 120 min.

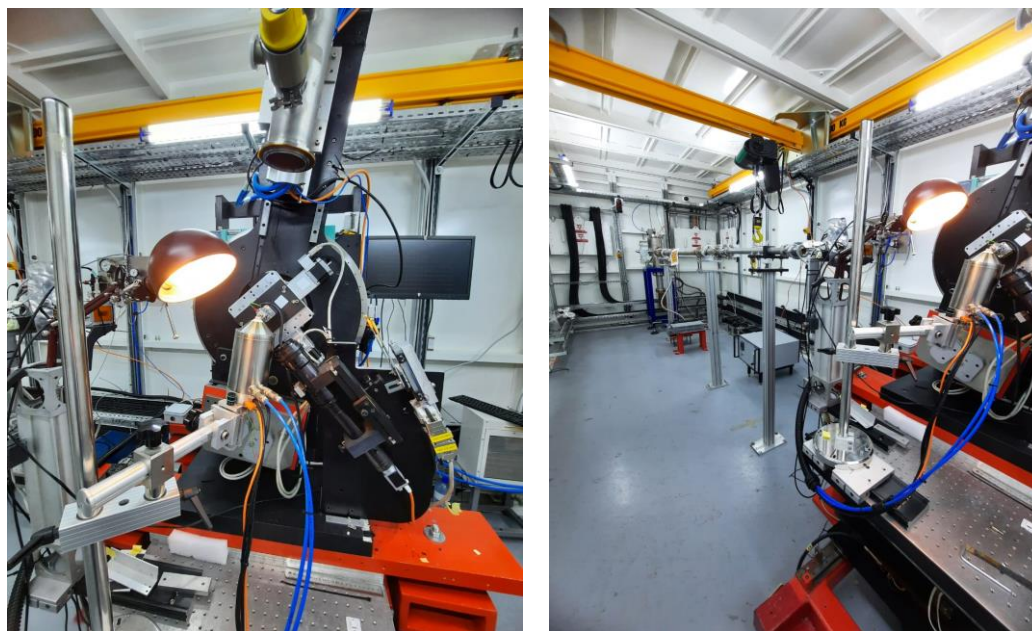


Figure 3.12: The experimental room at SESAME.

The cooling rate was as shown in Table 3.2:

Table 3.2: The cooling rate for the samples studied at high temperature.

Temperature (°C)	Time
556.0	16:07
487.4	16:20
394.2	16:39
333.4	16:51
276.2	17:03
226.0	17:13
202.4	17:17
135.4	17:30
91.0	17:41
75.6	17:46
56.3	17:55
45.9	18:02
40.4	18:07
33.4	18:17

- ✓ The wavelength of the beam in our experiment was:

$$\lambda = 1.033620 \text{ \AA}.$$

- ✓ All of the samples in literature were studied using conventional XRD device, so we should take advantage of Bragg's condition to figure out $2\theta_{\text{conventional}}$ as follows:

$$2\theta_{\text{conv.}} = \left(\frac{180}{3.14}\right) \times \sin^{-1} \left(1.4904897 \times \sin \left(2\theta_{\text{Synch.}} \times \left(\frac{3.14}{180}\right)\right)\right) \quad (10)$$

Chapter Four: Results and discussion

4.1 Structural properties for samples studied at RT

In this section, the X-ray powder diffraction results for each of Cr, Ni and In doped BZN studied at room temperature were analyzed. Their patterns are all shown in Figure 4.1. These samples were prepared previously in Marmara university laboratories in Turkey.

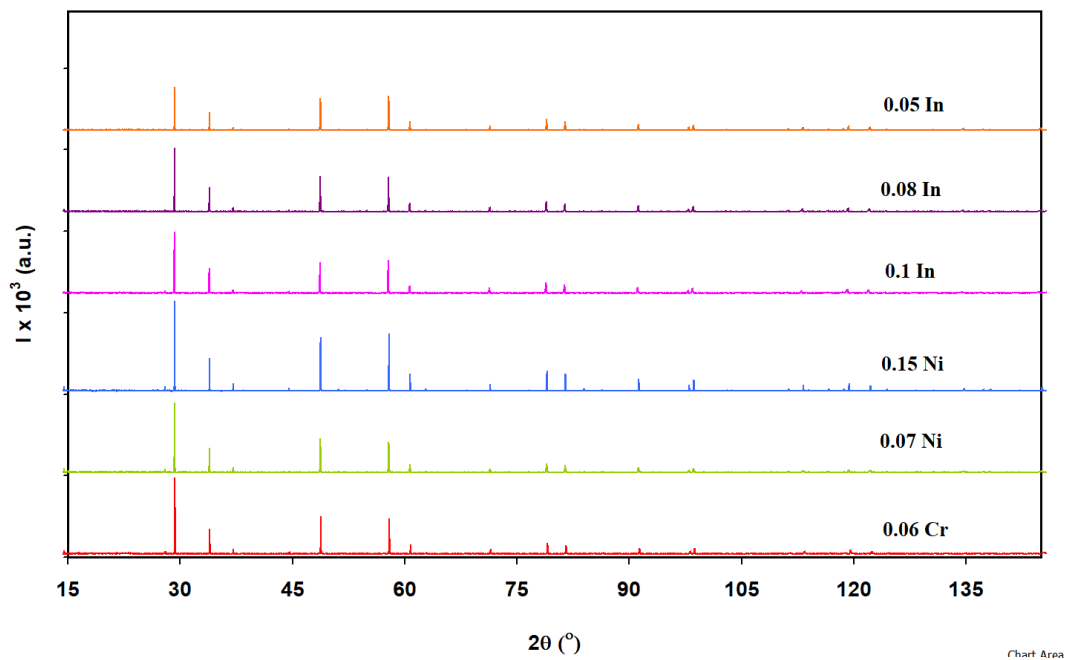


Figure 4.1: XRPD patterns of $\text{Bi}_{1.5}\text{Zn}_{0.92}\text{Nb}_{1.5}\text{O}_{6.92}$ pyrochlore doped with (Cr, Ni and In) at room temperature.

The results were analyzed after converting $\theta_{\text{synchrotron}}$ into $\theta_{\text{conventional}}$.

Comparing Fig. 4.1 with the XRPD pattern of the undoped BZN from previous studies [13], [36] & [37], the following observations were obtained: the main peak in all XRPD patterns is a result of the reflection from the (222) plane, the value of the main peak is nearly $\sim 29.3^\circ$ which is consistent with the values of $2\theta_{\text{main}}$ for the doped BZN pyrochlores samples in Table 4.1.1, in $(10^\circ\text{-}80^\circ)$ 2θ range, the number and location of peaks in the undoped case

is consistent with the doped case, and finally, the figure shows the peaks in an additional 2θ range: (80° - 150°), 2θ values for the most distinguishable two peaks are $\sim 79.09128^\circ$ and $\sim 81.557^\circ$ respectively.

In case of Cr doped BZN pyrochlore, the solubility limit for Cr in the BZN is $x=0.15$ [13], which agrees with our results since no new peaks appear in our XRPD pattern. Similar results are observed for In doping which has a solubility limit of $x=0.12$ [6] and Ni having a solubility limit of $x=0.1$ [42].

Table 4.1 below shows the intensity of the main peak and 2θ for the main peak, as well as the interplaner spacing in the crystal. Substituting $n=1$, $\lambda=1.5406 \text{ \AA}$ and inserting θ_{main} from Table 4.1, the interplaner spacing was calculated by Bragg's equation:

$$2d \sin\theta = n\lambda$$

Table 4.1: Intensity of the main peak, 2θ of the main peak and the interplaner spacing for doped BZN pyrochlore ceramics as a function of doping level at room temperature.

Dopant	Doping level	Intensity I (a.u.) of the main peak	2θ ($^\circ$) of the main peak	Interplaner spacing d (nm)
Ni	0.07	4447	29.2805	0.304920
Ni	0.15	5710	29.2896	0.304827
In	0.05	2856	29.2805	0.304920
In	0.08	4068	29.2603	0.305126
In	0.1	3982	29.2492	0.305239
Cr	0.06	4865	29.3098	0.304622

The mechanical properties such as lattice constant (a), crystalline size (D), strain (ϵ) and dislocation density (δ), all of which are calculated from 2θ and FWHM. We used OriginLab

program to figure out FWHM for the main peak of XRPD patterns only, by fitting the peak to a Gaussian shape.

The lattice constants for the samples were calculated using the following equation for the cubic structures:

$$a = \frac{d}{(h^2+k^2+l^2)^{\frac{1}{2}}} \quad (11)$$

All results are tabulated in Table 4.2 below.

Table 4.2: Mechanical parameters for Cr, In and Ni doped BZN pyrochlores samples at room temperature.

Dopant	$2\theta_{\text{main}} (^{\circ})$	$\beta (^{\circ})$	$a(\text{A}^{\circ})$	$\epsilon(\mu)$	D(nm)	$\delta \times 10^{11} \text{ line/cm}^3$
0.15 Ni	29.2896	0.0275	10.5595	459	311.8541	2.09161
0.07 Ni	29.2805	0.0482	10.5627	805	177.9214	6.4258
0.10 In	29.2492	0.0431	10.5738	721	198.9605	5.13865
0.05 In	29.2805	0.0398	10.5627	665	215.4726	4.38126
0.08 In	29.2603	0.0444	10.5699	742	193.14	5.45304
0.06 Cr	29.3098	0.0376	10.5524	627	228.0953	3.90976

It was reported that the lattice constant in case of the undoped BZN sintered at 1000 C° for 4 hours is $a = 10.5616 \text{ A}^{\circ}$ [38]. In case of Ni doped BZN, increasing the Ni content decreases the lattice constant slightly which contradicts with a previous study [38], that is due to the high dislocation density in 0.07 Ni doped BZN pyrochlore sample. In case of In doped BZN, the lattice constant increases with increasing In content, which agrees with a previous research which suggested that this increment is due to the larger ionic radius of In

than that of Zn [6]. Another study demonstrated that doping BZN pyrochlore with Cr decreases that lattice constant since it has a smaller ionic radius than that of Nb [13].

The micro-strain was calculated using equation (7) in Chapter 2:

$$\varepsilon = \frac{\beta}{4\tan\theta}$$

The variations in the micro-strain that results from the change of the relative positions of materials' parts are shown in Table 4.2. Due to the change in the lattice constant, there will be strain in the lattice. The positive strain in the table tells us that the strain type is a stretching one, which leads to dislocations in the crystal lattice.

The crystalline size was calculated using equation (4) in Chapter 2:

$$D = \frac{K\lambda}{\beta\cos\theta}$$

Finally, the dislocation density was calculated in case of line defect using equation (6) in Chapter 2:

$$\delta = \frac{15\varepsilon}{aD}$$

As observed in Table 4.2, micro-strain and dislocation density decreases as the crystalline size increases, which suggests a fewer number of lattice imperfections [39]. That is because of the decrease in the grain boundaries occurrence.

4.2 Structural properties for samples studied at high HT (RT-600) C°

In this section, we will discuss the effect of temperature on each of the XRPD patterns, mechanical properties and peaks sites. Also, we will discuss the temperature factor role in appearance of new peaks, which returns to a certain phase material even if we are under the solubility limit. In this section, we discuss in details the structural properties of (0.10) Cr doped and (0.10) Ni doped samples.

4.2.1 (0.10) Cr doped BZN pyrochlore

Using OriginLab software, Fig. 4.2 shows a 3D Temperature dependent XRPD pattern from 50 C° to 600 C° in steps of 100 C°. Figure 4.3 shows an Excel plot of all patterns in steps of 25 C°. As we can see from both of the two figures, no new peaks have appeared with increasing temperature.

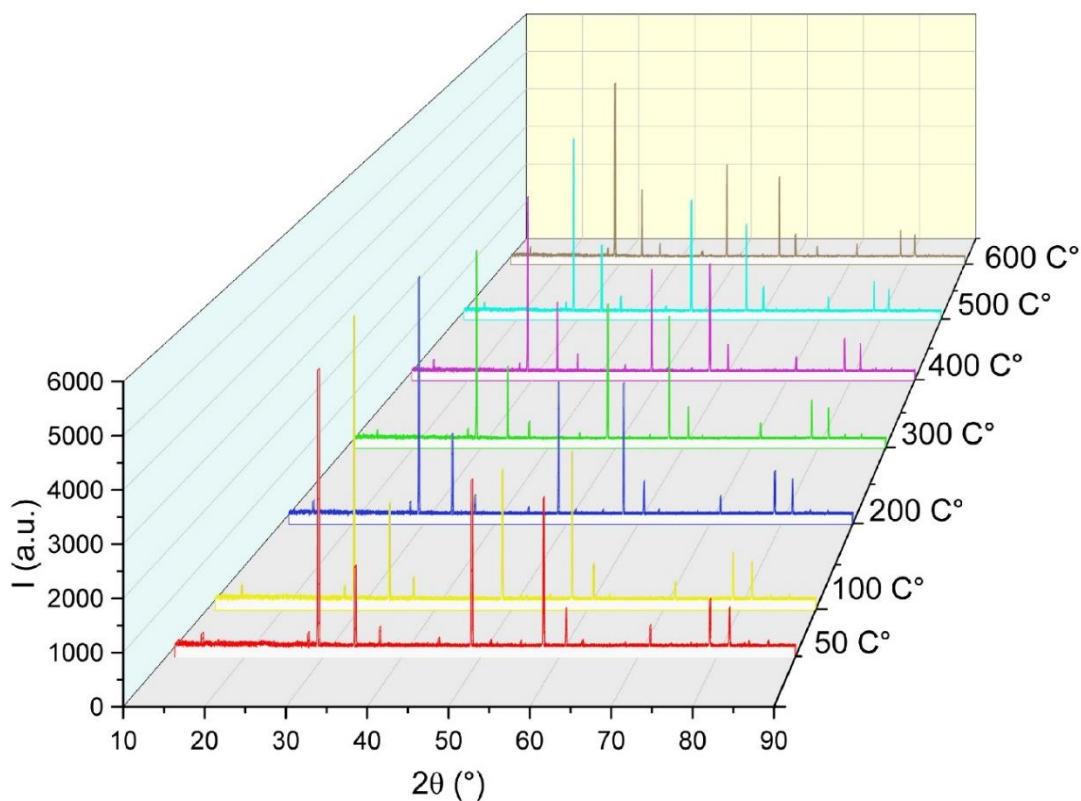


Figure 4.2: Three dimensional temperature dependent XRPD patterns of (0.10) Cr doped BZN pyrochlore from 50 C° to 600 C° in step of 100 C° and in 2θ range of (10°-90°).

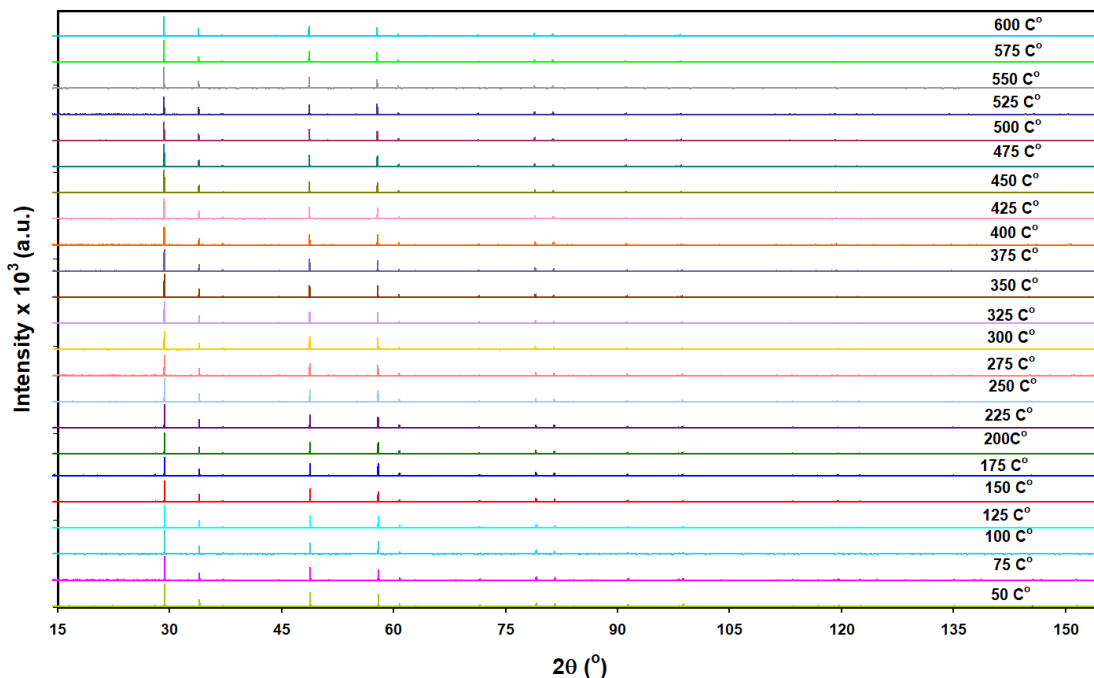


Figure 4.3: Temperature dependent XRPD patterns of (0.10) Cr doped BZN pyrochlore from 50 C° to 600 C° in step of 25 C° and in 2θ range of (15°-160°).

Zooming in on the main peak site in each pattern, we can observe that main peaks shift to lower angles with increasing temperature. This shift is clear in Fig. 4.4. As temperature increases, the interplaner spaces increase, hence theta decreases. So the main cause of the peak shift is the change in the lattice structure. Also, it was observed that for a certain peak, increasing temperature leads to a greater shift in the peak at higher Bragg angles. We also plotted $2\theta_{\text{main}}$ as a function of temperature in Fig. 4.5. We can notice the decrease in Bragg angle value with increasing temperature. At 50 °C it is 29.3209°, and at 600°C , it decreases to 29.2401°.

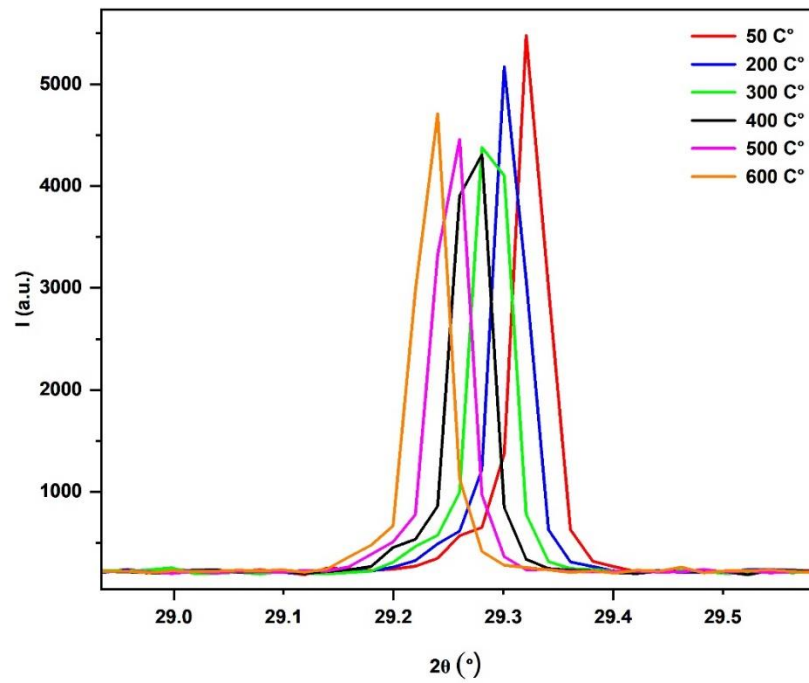


Figure 4.4: Zooming in on the main peaks of (0.10) Cr doped BZN pyrochlore sample for temperature range of (50-600) C°.

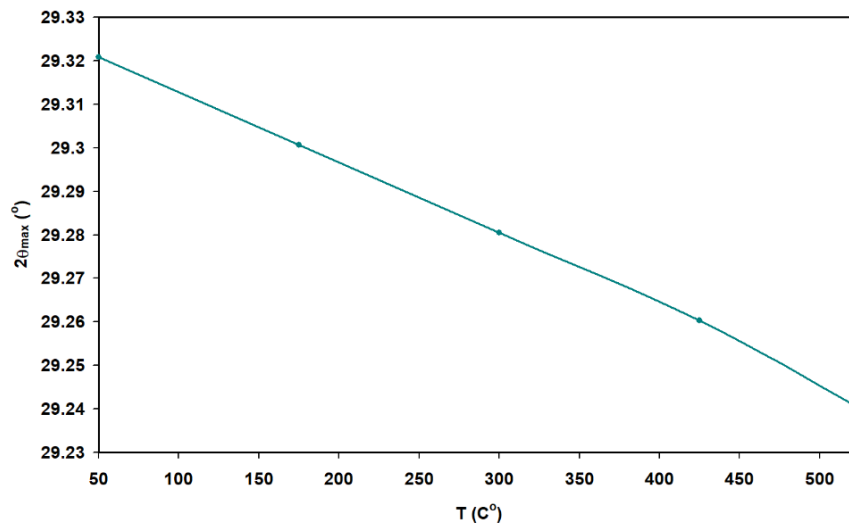


Figure 4.5: Main peak position ($2\theta_{\text{main}}$) vs temperature (T) in a temperature range of (50-525) °C for (0.10) Cr doped BZN pyrochlore ceramic.

Figure 4.6 below shows the intensity of the main peak, crystallite size, micro-strain, dislocation density, lattice constant and interplaner spacing as a function of temperature in a range of (50-600) C° for (0.10) Cr doped BZN pyrochlore ceramic sample. In order to calculate these mechanical properties, OriginLab program was used to figure out FWHM for only the main peak of XRPD patterns, by fitting the peak to a Gaussian shape. Starting with the intensity of the main peak, the pattern is oscillatory observing that its peaks decrease with increasing temperature, the first peak has an intensity of 5790 (a.u.) while the last one has an intensity of 5311 (a.u.). That is due to the thermal vibrations of lattice atoms, the atoms in each plane are no longer in their initial places. In other words, the lattice planes were smeared out. The crystallite size has been calculated using Scherrer equation for all points. Knowing that there is a limitation imposed on this equation when the crystallite size is larger than 200 nm, the values in the pattern fluctuate around this value so this equation is valid to calculate the crystallite size.

Moving to the micro-strain, it is also an oscillatory property having positive values, meaning that the strain type is a stretching one, leading to dislocations in the crystal lattice. The oscillatory behavior in the patterns is due to the strain relief in the crystal. Any crystal will try to retain its own structure so it will not expand forever. An inverse relation between micro-strain and crystallite size is observed, the peak in the D vs T pattern is a trough in the micro-strain vs T pattern. The same inverse relation is between crystallite size and dislocation density [43]. As for the lattice constant values, they increase gradually as temperature increases from 10.5485 Å at 50 C° to 10.5770 Å at 600 C°, which insures the smearing out of the lattice planes and the shift to the lower angles with increasing temperature. Interplaner spacing increases from 0.304509 nm at 50 C° to 0.305332 nm at 600 C° for the same reason.

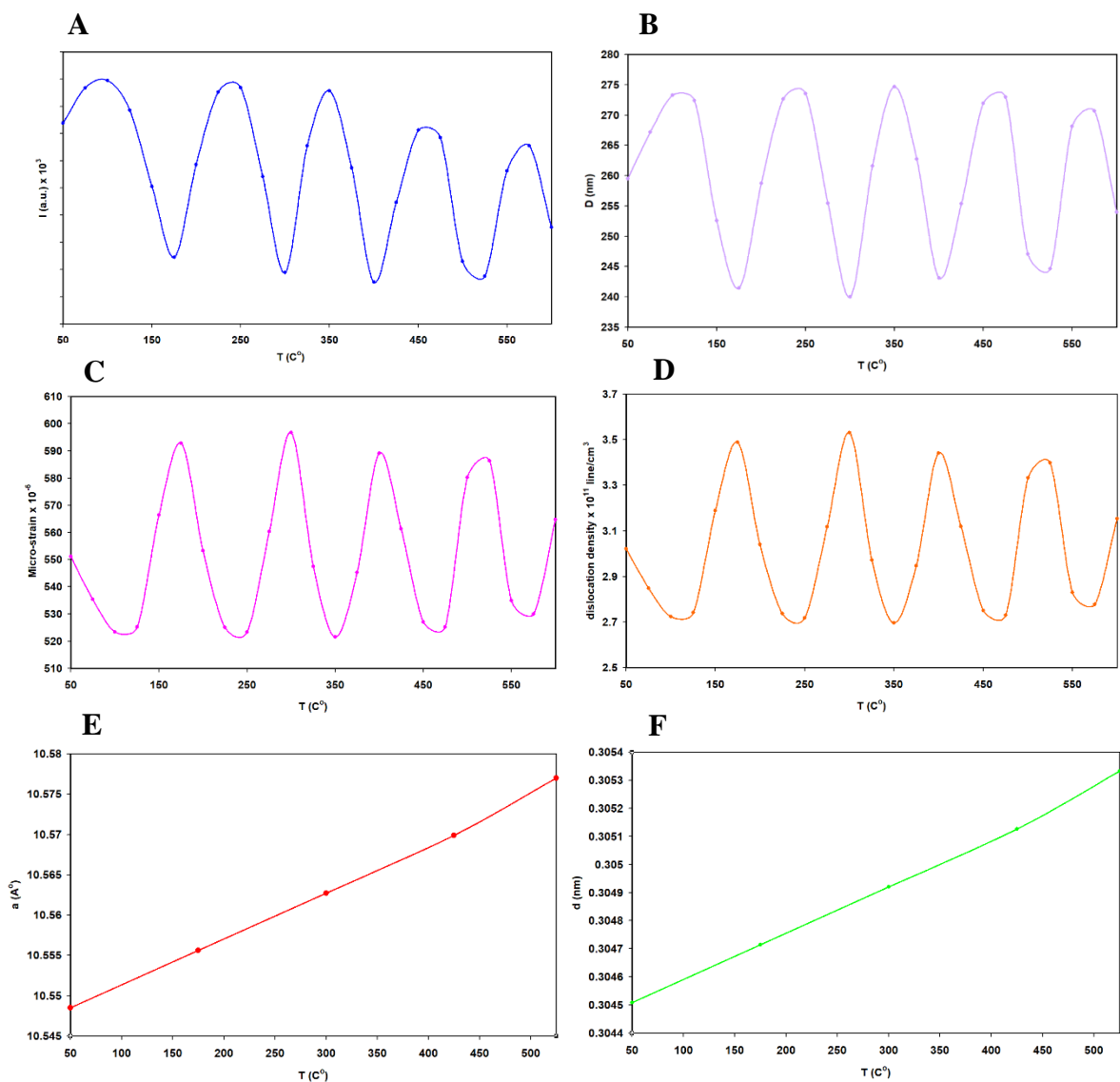


Figure 4.6: The variation of the: A. intensity of the main peak, B. crystallite size, C. micro-strain (μ), D. dislocation density δ , E. lattice constant and F. interplaner spacing with increasing temperature in a range of (50-600) °C of (0.10) Cr doped BZN pyrochlore

4.2.2 (0.10) Ni doped BZN

Using OriginLab software, Fig. 4.7 shows a 3D Temperature dependent XRPD pattern from 30 C° to 600 C° in steps of 100 C°. Figure 4.8 shows an Excel plot of all patterns in

steps of 25 C°. As we can see from both of the two figures, no new peaks have appeared as temperature increases until 575 C°, meaning that a single phase pyrochlore compound can be gained in this range of temperature indicating the thermal stability of Ni doped BZN pyrochlore up to 575 C°.

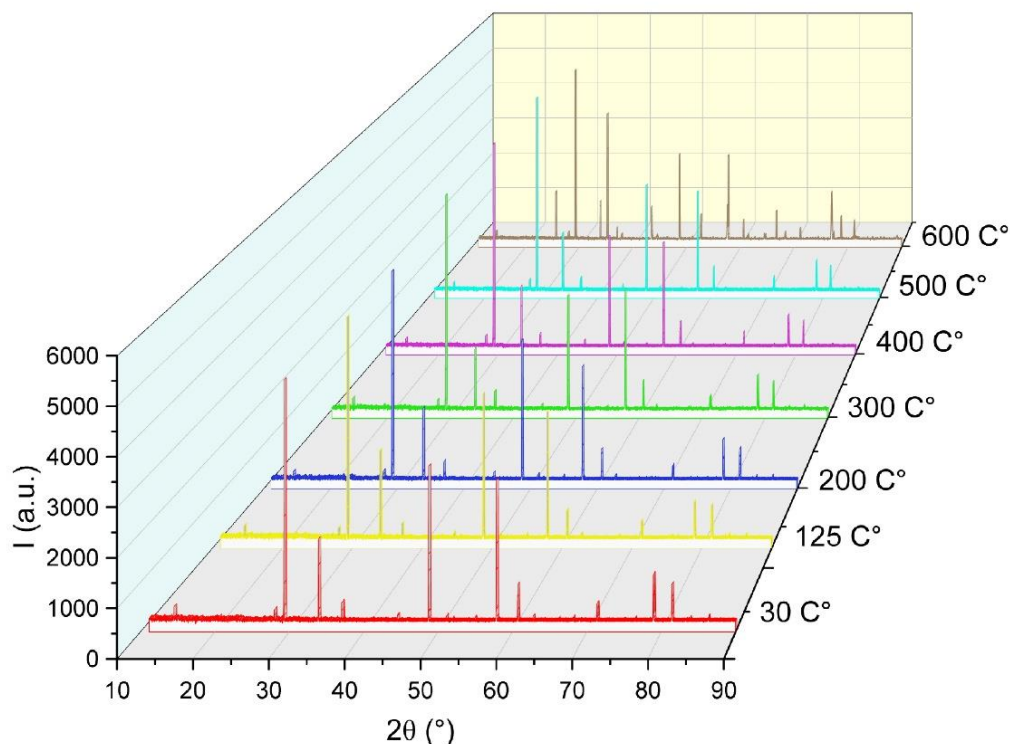


Figure 4.7: Three dimensional temperature dependent XRPD patterns from 30 C° to 600 C° in a step of 100 C° and in 2θ range of (10°-90°).

At 600 C°, seven new peaks have appeared at this temperature, which indicates the formation of new solid separated phases of certain materials. This suggests that increasing temperature decreased the solubility limit from 0.15 to one that is below 0.10 which is the Nickle content in the study. We can interpret the decrease in the solubility limit by recalling that the reaction is an exothermic one. These new peaks are represented by the red numbers in Fig. 4.9. We referred to relevant literature to specify the origin of these peaks.

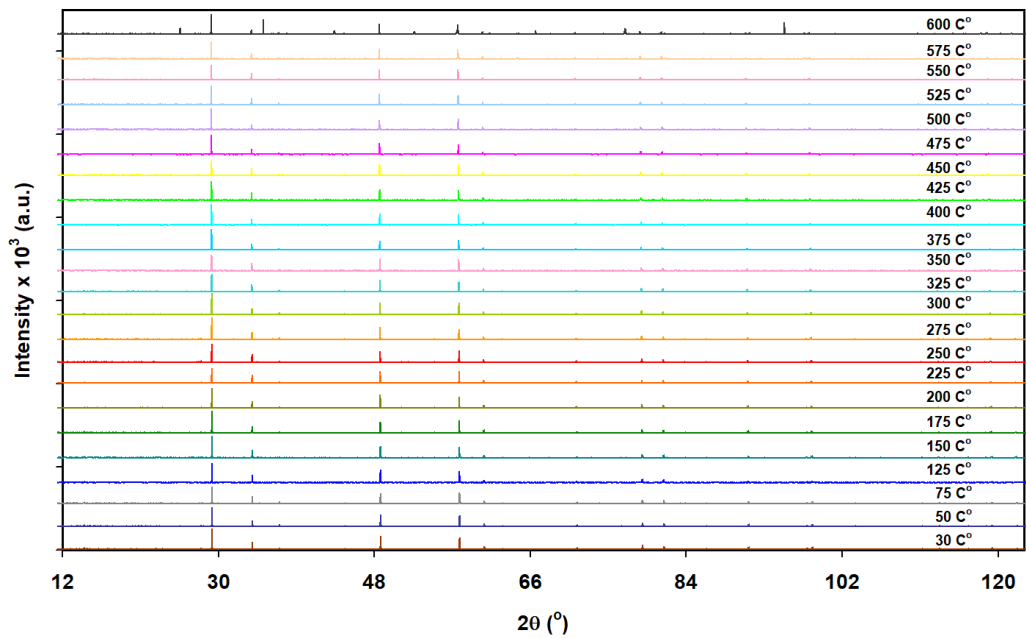


Figure 4.8: Temperature dependent XRPD patterns from 30 C° to 600 C° in a step of 25 C° and in 2θ range of (12°-125°).

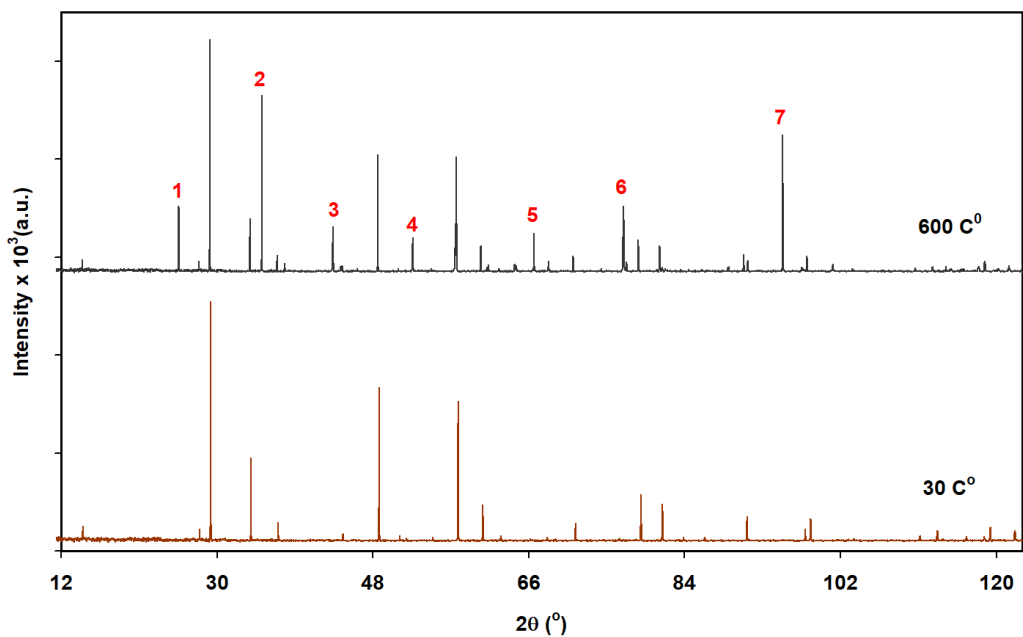


Figure 4.9: A comparison between the XRPD patterns of (0.10) Ni doped BZN at 30 C° and at 600 C° in 2θ range of (12°-125°).

All of the new peaks are tabulated in Table 4.3 below. Starting with the first new peak, it has 2θ of 25.57478° . It was reported that tetragonal Nb_2O_5 has a peak with high intensity at 2θ of nearly 25.70° [40], so the first peak may go back to this phase of material. Moving to the next new peak, which has 2θ of 35.17912° , the closest peak was for ZnO NPs having a hexagonal structure which was investigated to be 36.252° , which corresponds to the reflection from (101) plane [41]. The third peak has 2θ of 43.40210° , it is closed to the dominant 2θ for FCC NiO NPs which is equal to 42.76° based on a previous study [42], 43.290° in another study [43], and 43.14040° in a third study [44]. All of previous studies have reported the plane of reflection to be (200). The rest of the seven new peaks are due to dislocations and stacking faults in the crystal structure of the sample.

Table 4.3: Shows the origin of the seven new peaks appeared in the XRPD pattern at 600°C for (0.10) Ni doped BZN pyrochlore ceramic sample.

Peak number	2θ ($^\circ$)	Related Intensity (a.u.)	Material	Crystal structure	Space group
1	25.57478	1546.7120	Nb_2O_5	Tetragonal	14/mmm
2	35.17912	3725.9720	ZnO	Hexagonal	P63mc
3	43.40210	1116.7550	NiO	FCC	Fm3m
4	52.60903	897.9901	Unknown	-	-
5	66.61307	991.960	Unknown	-	-
6	76.94071	1540.0630	Unknown	-	-
7	95.34664	2990.430	Unknown	-	-

Zooming in again on the main peak site in each pattern, we can notice that main peaks shift to lower angles with increasing temperature. This shift is clear in Fig. 4.10. As temperature increases, the interplaner spacing increase, hence, theta decreases. As we said before, the main cause of the peak shift is the change in the lattice structure. Again, we plot $2\theta_{\text{main}}$ as a function of temperature in Fig. 4.11. We can notice the decrease in Bragg angle value with increasing temperature from 29.2805° at 30°C to 29.1796° at 600°C .

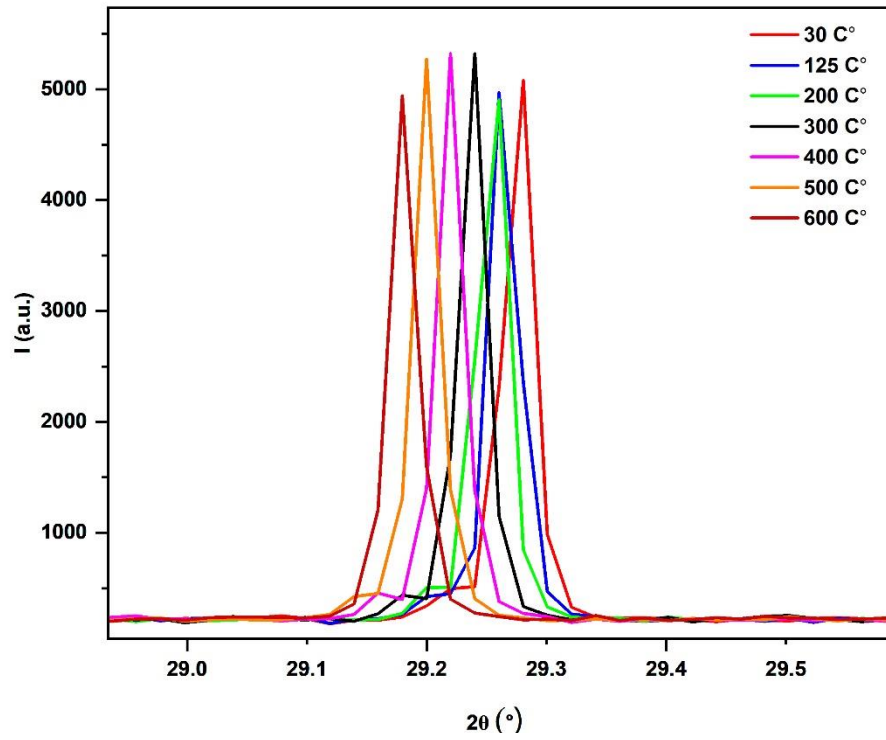


Figure 4.10: Zooming in on the main peaks of 0.1 Ni doped BZN pyrochlore sample for temperature range of (30-600) $^{\circ}\text{C}$.

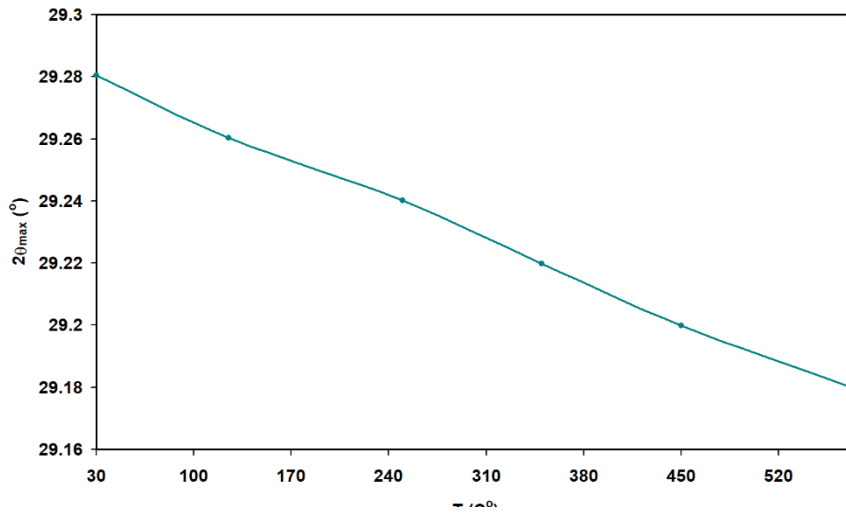


Figure 4.11: $2\theta_{\text{main}}$ vs T in a temperature range of (30-575) $^{\circ}\text{C}$ for (0.10) Ni doped BZN pyrochlore ceramic.

In Fig. 4.12, the same steps in plotting (0.10) Cr doped BZN pyrochlore ceramic in the previous subsection were followed. The figure shows the intensity of the main peak, crystallite size, micro-strain, dislocation density, lattice constant and interplaner spacing as a function of temperature in a range of (30-600) C° for (0.10) Ni doped BZN pyrochlore ceramic sample. Regarding the intensity of the main peak, it is oscillatory with increasing temperature as shown in pattern A. Again, the peak decreases with increasing temperature starting with 5449 (a.u.) at 150 C° and ending with 5271 (a.u.) at 500 C°. The crystallite size has been calculated using Scherrer equation for all points in pattern B except two point (at 425 C° and 500 C°), due to the limitation imposed on this equation when the size is larger than 200 nm where it exceeds this value for these two points. Otherwise, the equation is valid since the pattern fluctuate around 200 nm.

Micro-strain pattern is also oscillatory having positive values, meaning that the strain type is a stretching one, leading to dislocations in the crystal lattice. In addition, an inverse relation between micro-strain and crystallite size is observed, the peak in the D vs T pattern is a trough in the micro-strain vs T pattern. As for the lattice constant values, they increase gradually as temperature increases from 10.5627Å° at 30 C° to 10.5985Å° at 600 C°, which insures the smearing out of the lattice planes and the shift to the lower angles with increasing temperature. Interplaner spacing increases from 0.30492 nm at 30 C° to 0.30595 nm at 600 C°.

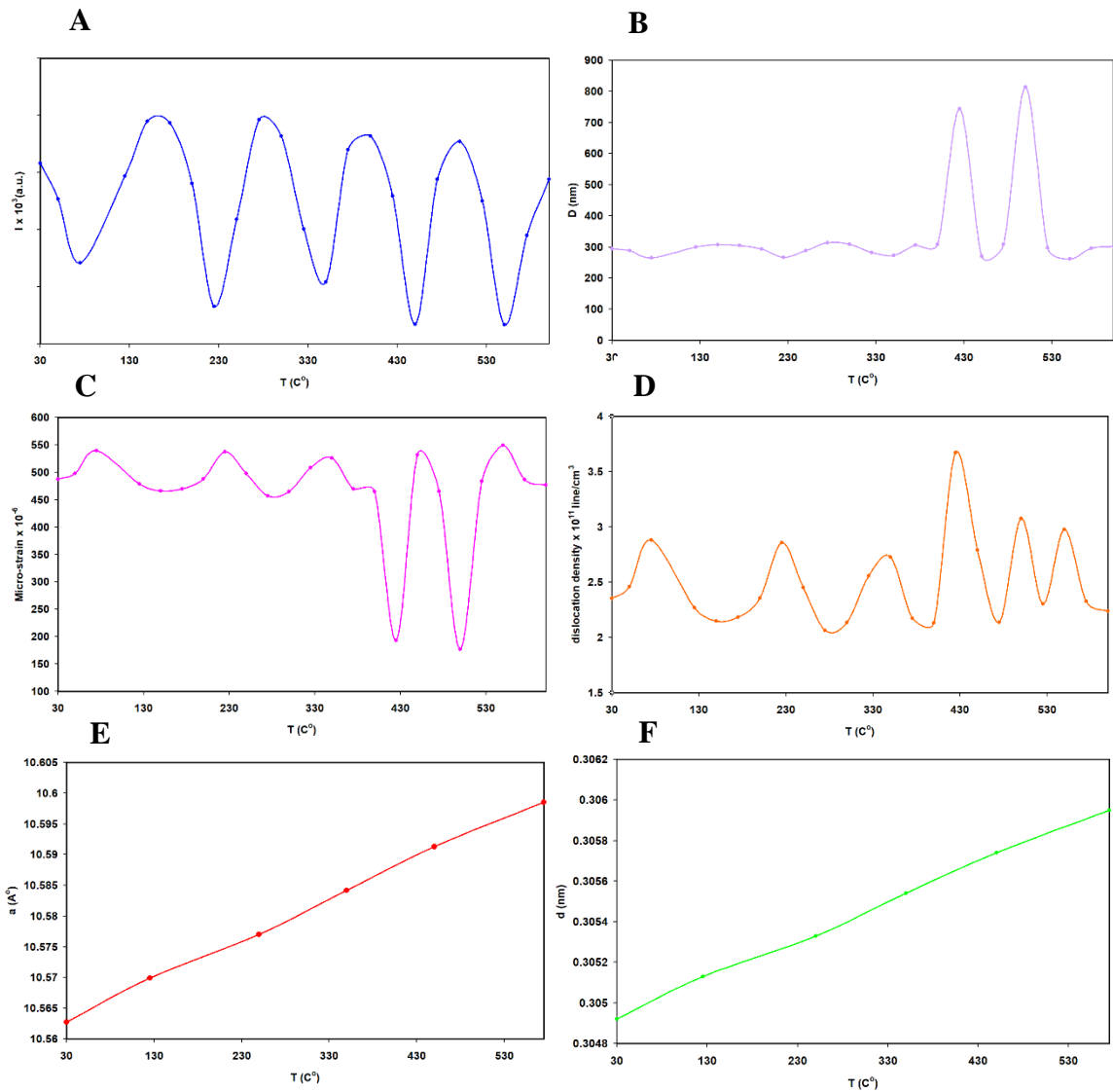


Figure 4.12: The variation of the: A. intensity of the main peak, B. crystallite size, C. micro-strain (μ), D. dislocation density δ , E. lattice constant and F. interplaner spacing with increasing temperature in a range of (30-600) °C of (0.10) Ni doped BZN pyrochlore ceramic.

4.3 Thermal Expansion Coefficient (TEC)

In order to figure out Thermal Expansion Coefficient for the samples studied at high temperatures up to 600 C°, the following equation was used:

$$\alpha = \left(\frac{1}{a_{50\text{ }^{\circ}\text{C}}} \right) \frac{(a_T - a_{50\text{ }^{\circ}\text{C}})}{(T - 50\text{ }^{\circ}\text{C})}$$

(12)

TEC value for (0.10) Cr doped BZN pyrochlore ceramic is $4.9124 \times 10^{-6} \left(\frac{1}{^{\circ}\text{C}} \right)$ and for (0.10) Ni doped BZN pyrochlore ceramic is $6.1623 \times 10^{-6} \left(\frac{1}{^{\circ}\text{C}} \right)$. The value of TEC for the second sample is higher than that for the first, which indicates that (0.10) Ni doped BZN sample expands more in the same temperature range. We can interpret this from the bond strength, Cr-O bond is stronger than Ni-O bond requiring higher temperature to expand.

Since TEC tells us how the growth of materials responds to the change in temperature, the low values for the two samples indicates that doped BZN pyrochlore ceramics expanded slowly with increasing temperature.

Chapter Five: Conclusions

In this thesis, we have considered the doping effect on the Cr, Ni and In doped BZN pyrochlore ceramics studied at RT. In addition, we have considered the effect of temperature on the (0.10) Cr and (0.10) Ni doped BZN pyrochlore ceramics studied in a temperature range of (RT-600) C° in a step of 25 C°. All of the samples were prepared through solid state reaction technique at which the oxides were mixed with ethyl alcohol after weighing in proper ratios. Then they were dried, calcined at 800 C° and re-milled. After that they were pressed into uniform pellets and sintered in a closed alumina crucible to prevent any evaporation losses. Finally, these pellets were crushed into fine powders.

All of the samples' structures were investigated in the MS/XRPD beamline at SESAME using synchrotron radiation. The results were studied after converting $\theta_{\text{synchrotron}}$ into $\theta_{\text{conventional}}$. XRPD technique enabled us to calculate the mechanical properties including each of the lattice constants, FWHM, micro-strain, crystallite size and dislocation density.

For the samples studied at RT, the XRPD patterns give an additional θ range that has not been reported in previous literature. No new phases have appeared since we are under the solubility limit for all samples. The lattice constant has a values of 10.5524, 10.5699, 10.5627, 10.5738, 10.5627 and 10.5595 Å for 0.06 Cr, 0.08 In, 0.05 In, 0.10 In, 0.07 Ni and 0.15 Ni doped BZN respectively. The increase in the lattice constant with increasing In content is due to the larger ionic radius of In than that of Zn. On the other hand, doping BZN pyrochlore with Cr decreases the lattice constant since it has a smaller ionic radius than that of Nb. Also, both of the micro-strain and dislocation density have an inverse relation with the crystallite size.

The samples studied at high temperature have shown remarkable results since (0.10) Ni doped BZN sample revealed new seven peaks in the XRPD pattern at 600 C°. We have used OriginLab program to plot a 3D temperature dependent XRPD patterns. With respect to (0.10) Cr doped BZN pyrochlore, no new peaks have appeared in (50-600) C° range of temperature indicating the thermal stability in this range. As temperature increases, maximum peak shifts to lower angles indicating increasing in the lattice constant value from 10.5485 Å to 10.5770 Å, which insures the smearing out of the lattice planes. In addition,

increasing the temperature generally decreases the intensities due to the thermal vibrations of the lattice atoms that are no longer in their initial positions. Also, increasing temperature leads to a greater shift in the peak at higher Bragg angles. Moving to (0.10) Ni doped BZN pyrochlore, no new peaks have appeared with increasing temperature until 575 C°. At 600 C°, the crystal structure is thermally not stable anymore since seven new peaks have appeared suggesting the formation of new separated phases, which indicated that increasing the temperature decreases the solubility limit to value less than 0.10. The values of 2θ for the new peaks are 25.57478°, 35.17912°, 43.40210°, 52.60903°, 66.61307°, 76.94071° and 95.34664°. The first three peaks are understood to arise from Nb₂O₅, ZnO, and NiO phases respectively, while the rest of the seven new peaks are due to dislocations and stacking faults in the crystal structure of the sample. The maximum peak shifting to lower angles have occurred again for this sample. Also, lattice constant value increases gradually as temperature increases from 10.5627Å to 10.5985 Å.

At the end, we have calculated the Thermal Expansion Coefficient for the samples studied at high temperature up to 600°C. It is $4.9124 \times 10^{-6} \left(\frac{1}{^\circ\text{C}}\right)$ for the (0.10) Cr doped BZN pyrochlore ceramic and $6.1623 \times 10^{-6} \left(\frac{1}{^\circ\text{C}}\right)$ for the (0.10) Ni doped BZN pyrochlore ceramic. In the future, we may try to reach temperatures higher than 600 C° when studying the thermal behavior for the doped BZN pyrochlore ceramics.

References

- Van Loef, E., Wang, Y., Glodo, J., Brecher, C., Lempicki, A, and Shah, K. S. (2008). Transparent ceramics based on pyrochlores. *Recent Advances in Ceramic Scintillators. MRS Proceedings, 1038*, (602).
- S.E. Al Garni, A.F. Qasrawi and A. Mergen. (2016). Physical properties of the $\text{Bi}_{1.5}\text{Zn}_{0.92}\text{-}2\text{xHf}_x\text{Nb}_{1.5}\text{O}_{6.92}$ solid solutions. *Ceramics International, 42*, 3372–3379.
- T. S. Kayed and A. Mergen. (2003). Electrical properties of $\text{Bi}_{1.5}\text{ZnSb}_{1.5}\text{O}_7$ pyrochlore ceramics. *Cryst. Res. Technol. 38*, (12), 1077 – 1081.
- Lirong Luo, Chunhui Xu, Xiaohong Chang, Fujian He, Xiacong Tian, Luhua Lu, Ying Chen, Shuen Hou and Hongyun Jin. (2020). Effect of CaO and CeO₂ co-doping on thermo-physical properties of $\text{La}_2\text{Zr}_2\text{O}_7$. *Journal of Asian Ceramic Societies 8*, (4), 1010-1017.
- Lei Guo, Mingzhu Li, Yu Zhang and Fuxing Ye. (2015). Improved Toughness and Thermal Expansion of Non-stoichiometry $\text{Gd}_{2-x}\text{Zr}_x\text{O}_{7+x/2}$ Ceramics for Thermal Barrier Coating Application. *Journal of Materials Science & Technology, 32*, (1), 28-33.
- Ayhan Mergen, Oguz Özyoldas and İbrahim Küçük. (2012). Production and properties of In and Ir doped $\text{Bi}_{1.5}\text{Zn}_{0.92}\text{Nb}_{1.5}\text{O}_{6.92}$ pyrochlores. *Journal of the European Ceramic Society, 32*, (9), 2019–2023.
- Ladislav Čelko, Serhii Tkachenko, Mariano CasasLuna , Lucie Dyčková, Vendula Bednaříková, Michaela Remešová, Pavel Komarov, Andrea Deák, Matej Baláž, Deborah Crawford , Sebastian Diaz-de-la-Torre, Ede Bodoki and Jaroslav Cihlář. (2022). High-energy ball milling and spark plasma sintering of molybdenum - lanthanum oxide ($\text{Mo-La}_2\text{O}_3$) and molybdenum – lanthanum zirconate ($\text{Mo-La}_2\text{Zr}_2\text{O}_7$) composite powders. *International Journal of Refractory Metals and Hard Materials, 102*, 105717.
- Atef F. Qasrawi, Mays A. Abdalghafour and A. Mergen. (2020). Tungsten doped $\text{Bi}_{1.5}\text{Zn}_{0.92}\text{Nb}_{1.5}\text{O}_{6.92}$ ceramics designed as radio/microwave band pass/reject filters. *Microwave and Optical Technology Letters, 63*, 1101-1105.
- K SUDHEENDRAN and PAULA M VILARINHO. (2020). Electrophoretic deposition of $\text{Bi}_{1.5}\text{Zn}_{1.0}\text{Nb}_{1.5}\text{O}_7$ thick films on metal foils for flexible electronic devices. *Bull Mater Sci, 43*, 303.
- Ding Shihua, Song Tianxiu, Zhang Qian, Huang Long and Zhang Xioyun. (2018). Structure and dielectric properties of Ru doped $\text{Bi}_{1.5}\text{ZnNb}_{1.5}\text{O}_7$ ceramics. *Ceramics International, 44*, S58-S60.
- Qianyu Guo, Lingxia Li, Shihui Yu, Zheng Sun, Haoran Zheng and Weijia Luo. (2018). Temperature–stable dielectrics based on Ni–doped $\text{Bi}_2\text{Zn}_2/3\text{Nb}_4/3\text{O}_7$ pyrochlore ceramics for low temperature co-fired ceramic. *Journal of Alloys and Compounds, 767*, 259-263.
- A. F. Qasrawi, Mays A. Abdalghafour and A. Mergen. (2021). Structural, Optical and Electrical Properties of $\text{Bi}_{1.5}\text{Zn}_{0.92}\text{Nb}_{1.5-6x/5}\text{W}_x\text{O}_{6.92}$ Pyrochlore Ceramics. *Materials Research, 24*, (2).

A. Mergen, H. Zorlu, M. Özdemir and M. Yumak. (2011). Fabrication and characterization of Cr and Co doped $\text{Bi}_{1.5}\text{Zn}_{0.92}\text{Nb}_{1.5}\text{O}_{6.92}$ pyrochlores. *Journal of the European Ceramic Society*, 31, (14), 2633-2639.

George Karadimas and Konstantinos Salonitis. (2023). Ceramic Matrix Composites for Aero Engine Applications—A Review. *Applied Sciences*, 13, (5), 3017.

Askeland, D. (2010). Ceramic Materials. *THE SCIENCE AND ENGINEERING OF MATERIALS: Properties of Ceramics*, (574).

Li, W., Zhou, D., Xu, R., Wang, D.-W., Su, J., Pang, L.-X., Chen and G.-H.. (2019). BaTiO₃-Based Multilayers with Outstanding Energy Storage Performance for High Temperature Capacitor Applications. *ACS Appl. Energy Mater*, 2, (8), 5499–5506.

Kamutzki, Franz. (2023). Synthesis and characterisation of silicate ceramics for dielectric and magnetic applications. *Advanced Ceramic Materials Series*, 10, 2569-8338.

Angela Pirri, Roman N. Maksimov, Jiang Li, Matteo Vannini and Guido Toci. (2022). Achievements and Future Perspectives of the Trivalent Thulium-Ion-Doped Mixed-Sesquioxide Ceramics for Laser Applications. *Materials*, 15, (6), 2084.

Qiong Liu, Zhouyao Li, Jiang Li, Faqi Zhan, Di Zhai, Qiwei Sun, Zhida Xiao, Hang Luo and Dou Zhang. (2022). Three dimensional BaTiO₃ piezoelectric ceramics coated with TiO₂ nanoarray for high performance of piezo-photoelectric catalysis. *Nano Energy*, 98, 2211-2855.

Maziar Montazerian, Francesco Baino, Elisa Fiume, Carla Migneco, Amirhossein Alaghmandfar, Omid Sedighi, Anthony V. DeCeanne, Collin J. Wilkinson and John C. Mauro. (2023). Glass-ceramics in dentistry: Fundamentals, technologies, experimental techniques, applications, and open issues. *Progress in Materials Science*, 132, 101023.

Wanhyuk Chang, Eun Heui Kang, Heon Jun Jeong, Wonjoon Choi and Joon Hyung Shim. (2023). Inkjet printing of perovskite ceramics for high-performance proton ceramic fuel cells. *Energy*, 268, 126489.

Askeland, D. (2010). Ceramic Materials. *THE SCIENCE AND ENGINEERING OF MATERIALS: Applications of Ceramics*, (572).

Timothy Connor, Oskar Cheong, Thomas Bornhake, Alison C. Shad, Rebekka Tesch, Mengli Sun, Zhengda He, Andrey Bukayemsky, Victor L. Vinograd, Sarah C. Finkeldei and Piotr M. Kowalski. (2021). Pyrochlore Compounds From Atomistic Simulations. *Frontiers in Chemistry*, 9, 733321.

<https://www.flowcapture.com/>.

Arbel Haim. (2010). *Elastic and Mechanical Characterization of Thin Gold Films Utilizing Laser-Based Surface-Acoustic-Waves Spectroscopy*. [MS Thesis, Tel-Aviv University]. Palestine.

Camelia V. Stan, Christine M. Beavers ID, Martin Kunz and Nobumichi Tamura. (2018). X-Ray Diffraction under Extreme Conditions at the Advanced Light Source. *Quantum Beam Science*, 2, (4), 3390.

Cameron F. Holder, Raymond E. Schaak. (2019). Tutorial on Powder X-ray Diffraction for Characterizing Nanoscale Materials. *ACS Nano*, 13, (7), 7359–7365.

Siti Fatimah, Risti Ragadhita, Dwi Fitria Al Husaeni and Asep Bayu Dani Nandiyanto. (2021). How to Calculate Crystallite Size from X-Ray Diffraction (XRD) using Scherrer Method. *ASEAN Journal of Science and Engineering*, 2, (1), 65-76.

Jaspreet Nagra. (2019). *Modelling Microstructure-Property Relationships in Polycrystalline Metals using New Fast Fourier Transform- Based Crystal Plasticity Frameworks*. [PhD Thesis, University of Waterloo]. Canada.

Askeland, D. (2010). Mechanical Properties: Part One. *THE SCIENCE AND ENGINEERING OF MATERIALS: The Tensile Test: Use of the Stress–Strain Diagram*, (206).

<https://www.ansto.gov.au/about/locations/visit-australian-synchrotron>.

<https://www.sesame.org.jo/accelerators>.

T. Zolkin. (2017). Sector magnets or transverse electromagnetic fields in cylindrical coordinates. *Physical Review Accelerators and Beams*, 20, (4), 043501.

D. Krestou, A. Papagiannaki, M. Maropoulos and S. An. (2022). An Overview of the Production of Magnetic Core-Shell Nanoparticles and Their Biomedical Applications. *Metals*, 12, (4), 605.

Askeland, D. (2010). Atom and Movements in Materials. *THE SCIENCE AND ENGINEERING OF MATERIALS: Diffusion and Materials Processing*, (183).

Sonia Maria Zanettia and Sandra Andréia da Silvab. (2007). Synthesis and Characterization of Bismuth Zinc Niobate Pyrochlore Nanopowders. *Materials Research*, 10, (3), 261-266.

Hong Wang, Ralf Elsebrock, Theodor Schneller, Rainer Waser and Xi Yao. (2004). Bismuth zinc niobate (Bi_{1.5}ZnNb_{1.5}O₇) ceramics derived from metallo-organic decomposition precursor solution. *Solid State Communications*, 132, (7), 481–486.

A. F. Qasrawi, E. M. Nazzal and A. Mergen. (2012). Structural, optical, electrical and dielectric properties of Bi_{1.5}Zn_{0.92}Nb_{1.52}xNixO_{6.9223x/2} solid solution. *Advances in Applied Ceramics*, 111, (3), 165.

Anayara Begum, Amir Hussain and Atowar Rahman. (2012). Effect of deposition temperature on the structural and optical properties of chemically prepared nanocrystalline lead selenide thin films. *Beilstein J. Nanotechnol*, 3, (1), 438–443.

Ryoji Kodama, Yasuko Terada, Izumi Nakai, Shinichi Komaba and Naoaki Kumagaic. (2006). Electrochemical and In Situ XAFS-XRD Investigation of Nb₂O₅ for Rechargeable Lithium Batteries. *Journal of The Electrochemical Society*, 153, (3), 583-588.

Davood Raouf. (2013). Synthesis and microstructural properties of ZnO nanoparticles prepared by precipitation method. *Renewable Energy*, 50, 932-937.

Pawan Kumar Sharma, Manish Kumar Singh, Ganesh D. Sharma and Anupam Agrawal. (2021). NiO nanoparticles: Facile route synthesis, characterization and potential towards third generation solar cell. *Materials Today: Proceedings*, 43, (5), 3061-3065.

M. Alagiri, S. Ponnusamy and C. Muthamizhchelvan. (2012). Synthesis and characterization of NiO nanoparticles by sol–gel method. *J Mater Sci: Mater Electron*, 23, 728–732.

Ziad T. Khodair, Noor M. Ibrahim, Talib J. Kadhim and Ali M. Mohammad. (2022). Synthesis and characterization of nickel oxide (NiO) nanoparticles using an environmentally friendly method, and their biomedical applications. *Chemical Physics Letters*, 797, 139564.

التحليل البنائي لسيراميك BZN البيروكلوري المطعم كاقتران بدلالة الحرارة باستخدام شعاع السنكروترون.

راما واثق نجيب حثاوي

أ. د. عدلي صالح

أ. د. مؤيد أبو صاع

أ. د. زكي صالح

أ. د. محمد السعيد

ملخص

في هذه الأطروحة، تمت دراسة الخصائص البنائية لسيراميك BZN البيروكلوري الذي تم تطعيمه بكل من مادة الكروم والنيكل والإنديوم باستخدام إشعاع السنكروترون في مركز سيسامي للأبحاث. تمت دراسة التغيرات في البعد بين المستويات، ثابت البنينة، الانفعال المجهري، الحجم البلوري وكثافة الانخلاع. في الجزء الأول، تمت دراسة سيراميك BZN البيروكلوري المطعم في كل مرة بمادة الكروم، النيكل والإنديوم عند درجة حرارة الغرفة. قيمة ثابت البنينة تقل عند زيادة تركيز النيكل وتزداد عند زيادة تركيز الإنديوم في العينة. تمت ملاحظة أن زيادة ثابت البنينة مع زيادة تركيز المادة التي تم التطعيم بها يعود إلى الزيادة في نصف القطر الأيوني لهذه المادة. في حالة هذه العينات، لم تظهر أي قمم جديدة حيث أننا تحت مستوى حد الذائبية. في الجزء الثاني، تمت دراسة سيراميك BZN البيروكلوري المطعم بكل من (0.10) من الكروم و (0.10) من النيكل في نطاق درجة حرارة يتراوح بين (درجة حرارة الغرفة - 600) م° مع درجة زيادة مقدارها 25 م°. مع زيادة درجة الحرارة، انزاحت القمة القصوى نحو الزوايا الأقل مما سبب زيادة قيمة ثابت البنينة بالتدرج. كما أن زيادة درجة الحرارة بشكل عام قللت الشدة. بالإضافة إلى ذلك، زيادة درجة الحرارة أدت إلى زيادة الانزياح في القمة عند قيم زوايا براغ أعلى. قيمة ثابت البنينة زادت بالتدرج مع ازدياد درجة الحرارة من 10.5485 A° إلى 10.5770 A° في حالة سيراميك BZN البيروكلوري المطعم بتركيز (0.10) من الكروم، ومن 10.5627A° إلى 10.5985 A° في حالة سيراميك BZN البيروكلوري المطعم بتركيز (0.10) من النيكل. في حالة سيراميك BZN البيروكلوري المطعم بتركيز (0.10) من النيكل، ظهرت سبعة قمم XRPD جديدة ظهرت عند 25.57478°، 35.17912°، 43.40210°، 52.60903°، 66.61307°، 76.94071° و 95.34664°. أول ثلاثة قمم تم إيجاد أنها تعود إلى Nb_2O_5 ، ZnO و NiO بالترتيب، بينما باقي القمم تعود إلى الانخلاعات وأخطاء التراص في البنينة البلورية للعينة. وأخيراً، تم حساب معامل التمدد الحراري للعينات التي تمت دراستها عند درجات حرارة عالية لتكون قيمته $4.9124 \times 10^{-6} \left(\frac{1}{\text{م}}\right)$ حالة سيراميك BZN البيروكلوري المطعم بتركيز (0.10) من الكروم، و $6.1623 \times 10^{-6} \left(\frac{1}{\text{م}}\right)$ في حالة سيراميك BZN البيروكلوري المطعم بتركيز (0.10) من النيكل.

الكلمات المفتاحية: السيراميك البيروكلوري، XRPD، إشعاع السنكروترون، معامل التمدد الحراري.